Genetic analysis of right heart structure and function in 40,000 people

BioBank Japan Project; Pirruccello, James P.; Di Achille, Paolo; Nauffal, Victor; Nekoui, Mahan; Friedman, Samuel F.; Klarqvist, Marcus D. R.; Chaffin, Mark D.; Weng, Lu-Chen; Cunningham, Jonathan W.

Published in:
Nature genetics

DOI:
10.1038/s41588-022-01090-3

Publication date:
2022

ARTICLES
https://doi.org/10.1038/s41588-022-01090-3

nature genetics

Genetic analysis of right heart structure and function in 40,000 people

James P. Pirruccello[1,2,3,4,46], Paolo Di Achille[3,5,46], Victor Nauffal[3,6,46], Mahan Nekoui[3,4], Samuel F. Friedman[3,5], Marcus D. R. Klarqvist[3,5], Mark D. Chaffin[3], Lu-Chen Weng[3], Jonathan W. Cunningham[3,6], Shaan Khurshid[1,2,3,4], Carolina Roselli[3,7], Honghuang Lin[8,9], Satoshi Koyama[2,3,10], Kaoru Ito[10], Yoichiro Kamatani[11,12], Issei Komuro[13], The BioBank Japan Project*, Sean J. Jurgens[3,14], Emelia J. Benjamin[8,15,16], Puneet Batra[5], Pradeep Natarajan[1,2,3,4], Kenney Ng[17], Udo Hoffmann[18,19], Steven A. Lubitz[1,2,3,4,20], Jennifer E. Ho[4,21], Mark E. Lindsay[1,2,3,4,22], Anthony A. Philippakis[5] and Patrick T. Ellinor[1,2,3,4,20] ✉

Congenital heart diseases often involve maldevelopment of the evolutionarily recent right heart chamber. To gain insight into right heart structure and function, we fine-tuned deep learning models to recognize the right atrium, right ventricle and pulmonary artery, measuring right heart structures in 40,000 individuals from the UK Biobank with magnetic resonance imaging. Genome-wide association studies identified 130 distinct loci associated with at least one right heart measurement, of which 72 were not associated with left heart structures. Loci were found near genes previously linked with congenital heart disease, including *NKX2-5*, *TBX5/TBX3*, *WNT9B* and *GATA4*. A genome-wide polygenic predictor of right ventricular ejection fraction was associated with incident dilated cardiomyopathy (hazard ratio, 1.33 per standard deviation; $P = 7.1 \times 10^{-13}$) and remained significant after accounting for a left ventricular polygenic score. Harnessing deep learning to perform large-scale cardiac phenotyping, our results yield insights into the genetic determinants of right heart structure and function.

The heart evolved hundreds of millions of years ago as a tubular organ[1]. Septation of the main pumping chamber of the heart into distinct left and right ventricles evolved later in birds, mammals and some reptiles, and is under the control of conserved transcription factors such as TBX5 (ref. [2]). Enhanced delivery of oxygen to the systemic circulation—and to the heart itself—is the putative advantage of this separation of the circulatory system into a left-heart-driven systemic circuit and a right-heart-driven pulmonary circuit[3].

Left and right heart structures are derived from different progenitor cell populations and operate under different pressure regimes: the left heart faces high afterload, while the right heart generally faces relatively low afterload. During embryogenesis, the left ventricle (LV) forms from the first heart field, while the right ventricle (RV), the outflow tract and portions of the atria form from the second heart field[4–7]. Septation of the bilateral ventricular outflow tracts and the truncus arteriosus into the aorta and pulmonary artery (PA) also requires neuroectodermal neural crest cells[8–10].

The distinct embryological origins of the right and left ventricles probably contribute to the occurrence of right heart-predominant pathologies. These include various types of arrhythmogenic right ventricular cardiomyopathy (ARVC)[11–16], Brugada syndrome[17] and pulmonary hypertension. In addition, right ventricular dysfunction can be an important determinant of outcomes for individuals with heart failure syndromes[18–20].

A large-scale epidemiological analysis of right ventricular structure and function has been conducted using deep learning-derived cardiac measurements[21,22]. The distinct pathologies, embryology and physiology of the right heart motivated our efforts to quantify right heart structure and function, and to probe the common genetic basis for their variation.

[1]Cardiology Division, Massachusetts General Hospital, Boston, MA, USA. [2]Cardiovascular Research Center, Massachusetts General Hospital, Boston, MA, USA. [3]Cardiovascular Disease Initiative, Broad Institute of MIT and Harvard, Cambridge, MA, USA. [4]Harvard Medical School, Boston, MA, USA. [5]Data Sciences Platform, Broad Institute of MIT and Harvard, Cambridge, MA, USA. [6]Division of Cardiovascular Medicine, Brigham and Women's Hospital, Boston, MA, USA. [7]University Medical Center Groningen, University of Groningen, Groningen, The Netherlands. [8]Framingham Heart Study, Boston University and National Heart, Lung, and Blood Institute, Framingham, MA, USA. [9]Division of Clinical Informatics, Department of Medicine, University of Massachusetts Chan Medical School, Worcester, MA, USA. [10]Laboratory for Cardiovascular Genomics and Informatics, RIKEN Center for Integrative Medical Sciences, Kanagawa, Japan. [11]Laboratory of Complex Trait Genomics, Department of Computational Biology and Medical Sciences, Graduate School of Frontier Sciences, The University of Tokyo, Tokyo, Japan. [12]Laboratory for Statistical and Translational Genetics, RIKEN Center for Integrative Medical Sciences, Kanagawa, Japan. [13]Department of Cardiovascular Medicine, Graduate School of Medicine, The University of Tokyo, Tokyo, Japan. [14]Department of Experimental Cardiology, Amsterdam UMC, University of Amsterdam, Amsterdam, The Netherlands. [15]Department of Medicine, Cardiology and Preventive Medicine Sections, Boston University School of Medicine, Boston, MA, USA. [16]Epidemiology Department, Boston University School of Public Health, Boston, MA, USA. [17]IBM Research, Cambridge, MA, USA. [18]Department of Radiology, Harvard Medical School, Boston, MA, USA. [19]Cardiovascular Imaging Research Center, Massachusetts General Hospital, Boston, MA, USA. [20]Demoulas Center for Cardiac Arrhythmias, Massachusetts General Hospital, Boston, MA, USA. [21]CardioVascular Institute and Division of Cardiology, Department of Medicine, Beth Israel Deaconess Medical Center, Boston, MA, USA. [22]Thoracic Aortic Center, Massachusetts General Hospital, Boston, MA, USA. [46]These authors contributed equally: James P. Pirruccello, Paolo Di Achille, Victor Nauffal. * A list of authors and their affiliations appears at the end of the paper. ✉e-mail: ellinor@mgh.harvard.edu

In this work, we developed deep learning models to determine the dimensions and function of the right atrium (RA), the RV and the PA in up to 45,000 UK Biobank participants. We then evaluated the epidemiologic associations, pathologic outcomes and common genetic basis for variation in these right heart structures.

Results

Deep learning with cardiovascular magnetic resonance images. We derived right heart measurements in the UK Biobank imaging substudy of over 45,000 people[23–25] using deep learning models[26,27] trained on magnetic resonance images that were annotated manually by cardiologists (Fig. 1)[24]. We randomly selected 714 short axis images (out of over 24 million) and 445 four-chamber long axis images (out of over 2.2 million) for annotation. U-Net-derived deep learning models were then trained from these data[26,28–30]. The deep learning models were then used to produce pixel labels for the remaining images. Model construction, training and quality assessment are detailed in Methods and the Supplementary Note[31,32].

Reconstruction of right heart structures from deep learning. The deep learning model output was then postprocessed to extract measurements of the RA, the ventricles and the PA (Supplementary Note). In total, we were able to measure at least one cardiac structure in 45,504 individuals, of whom 41,135 contributed to at least one genome-wide association study after genotyping quality control and exclusion for prevalent disease (Table 1 and Supplementary Fig. 1). The mean and s.d. of the right atrial area measurements, right ventricular volumes and PA diameters are visualized in Supplementary Fig. 2. Standard values aggregated by sex for each of the phenotypes are reported in Supplementary Table 1, and by age bands and sex in Supplementary Table 2. Cross-correlation between left- and right-heart structures is represented in Supplementary Fig. 3 and described in the Supplementary Note.

To provide a direct comparison with left heart structures within the same sample, we also measured the left ventricle from short axis images. Left ventricular measurements included end diastolic volume (LVEDV), end systolic volume (LVESV), stroke volume (LVSV) and ejection fraction (LVEF). We compared PA measurements with previously reported aortic diameter measurements (Supplementary Note)[33].

Prevalent cardiovascular diseases linked to the right heart. We tested for correlations between right heart phenotypes and disease. These included analyses of hundreds of PheCode-based diseases prevalent at the time of imaging (Fig. 2 and Supplementary Table 3) and an analysis of three curated diseases with established chamber-specific links to the right heart diagnosed after imaging (atrial fibrillation, congestive heart failure and pulmonary hypertension; Supplementary Table 4)[20,34,35]. We also probed the properties of right ventricular volume throughout the cardiac cycle in the presence of congestive heart failure, pulmonary hypertension or noncardiac disease (Fig. 3 and Supplementary Fig. 4). Pre-existing pulmonary hypertension was associated with elevated right ventricular volumes even after accounting for the corresponding left ventricular volume, yielding a reduced right ventricular ejection fraction (RVEF; two-tailed $P = 3.9 \times 10^{-4}$ against the null hypothesis of no effect). Each of these findings is detailed in the Supplementary Note.

Heritability and genetic correlation of the right heart. The size-related phenotypes showed substantial heritability using BOLT-REML (as high as 0.36 for the maximum right atrial area, 0.41 for RV end diastolic volume (RVEDV), and 0.44 for the pulmonary root diameter)[36,37]. Heritabilities were lower for measurements of right heart function, such as RVEF, which had a heritability of 0.24 (Supplementary Table 5).

Table 1 | Participant characteristics

	Women	Men	All
n	21,946	19,189	41,135
Age at time of MRI	63.9 (7.6)	65.0 (7.8)	64.4 (7.7)
BMI (kg m^{-2})	26.0 (4.7)	26.9 (3.9)	26.4 (4.4)
Height (cm)	163 (6)	176 (7)	169 (9)
Weight (kg)	68.9 (13.1)	83.5 (13.3)	75.7 (15.0)
Systolic blood pressure (mmHg)	136 (19)	142 (17)	139 (19)
Diastolic blood pressure (mmHg)	77.1 (10.0)	80.9 (9.8)	78.9 (10.1)
Drinking status			
Current	20,134 (92 %)	18,020 (94 %)	38,154 (93 %)
Never	901 (4 %)	439 (2 %)	1,340 (3 %)
Prefer not to answer	7 (0 %)	12 (0 %)	19 (0 %)
Previous	747 (3 %)	604 (3 %)	1,351 (3 %)
Standard drinks/week	4.72 (5.32)	5.63 (6.80)	5.15 (6.08)
Smoking status			
Current	606 (3 %)	797 (4 %)	1,403 (3 %)
Never	14,343 (65 %)	11,296 (59 %)	25,639 (62 %)
Prefer not to answer	85 (0 %)	49 (0 %)	134 (0 %)
Previous	6,755 (31 %)	6,933 (36 %)	13,688 (33 %)
Smoking quantity (pack years)	3.40 (9.11)	5.43 (12.59)	4.35 (10.92)

Clinical characteristics of the 41,135 participants whose data contributed to at least one GWAS. For quantitative phenotypes, values shown represent mean (s.d.). For count data, values shown represent count (%). Cardiovascular phenotypes are detailed by age and sex in Supplementary Table 1.

We found strong genetic correlation between the right- and left-ventricular measurements ($r_g = 0.90$ between RVEDV and LVEDV; $r_g = 0.76$ between right ventricular end systolic volume (RVESV) and LVESV; and $r_g = 0.55$ between RVEF and LVEF)[37]. The proximal PA diameter had a genetic correlation of 0.63 with the ascending aortic diameter (Supplementary Table 6 and Supplementary Fig. 5).

Common variant genetic analysis of the right heart. To conduct genome-wide association studies (GWAS) of each trait, we excluded participants with diagnoses of heart failure, atrial fibrillation or myocardial infarction before their magnetic resonance imaging (MRI) study (participant characteristics in Table 1; sample exclusion flowchart in Supplementary Fig. 1). We conducted ten primary right heart GWAS: maximum and minimum right atrial area; RA fractional area change (FAC); RVESV, RVEDV, RVSV and RVEF; pulmonary root diameter and proximal PA diameter in systole and diastole (Manhattan plots in Fig. 4; quantile-quantile plots in Supplementary Fig. 6). We also evaluated PA strain and the body surface area (BSA)-indexed versions of all traits except for those that are dimensionless. Where paired left heart traits were available (such as LVEDV and RVEDV), we conducted within-sample GWAS of the left heart traits, and GWAS of right heart traits divided by their left heart counterparts. In total, we conducted 5 GWAS of right atrial phenotypes (Supplementary Fig. 7), 11 GWAS of right ventricular phenotypes (Supplementary Fig. 8) and 9 GWAS of pulmonary trunk phenotypes (Supplementary Fig. 9).

Up to 39,766 participants were included in the right heart GWAS (Supplementary Fig. 1), and we tested 11.6 million imputed SNPs with minor allele frequency (MAF) > 0.005. Additional GWAS

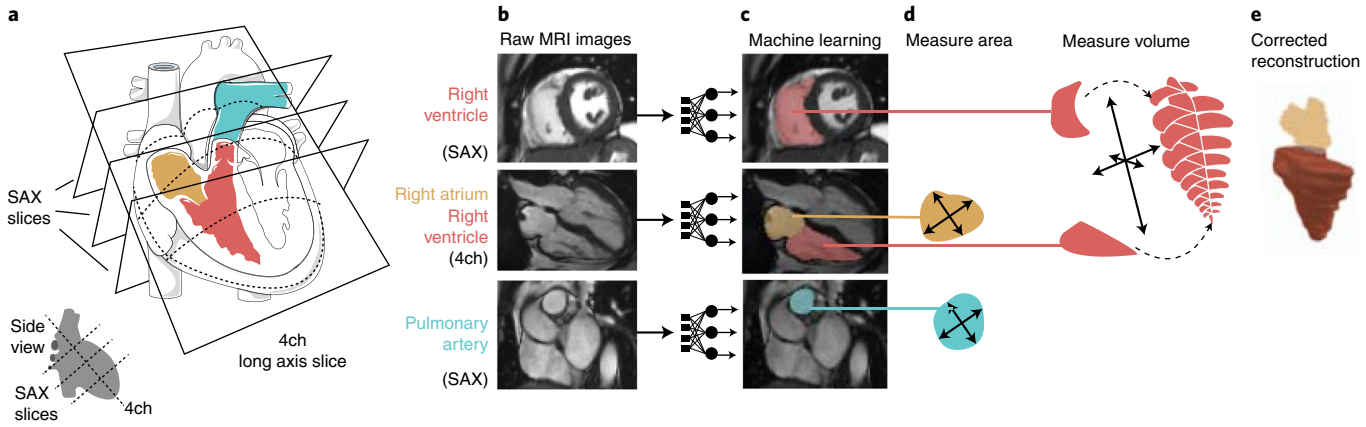

Fig. 1 | Right heart measurement with deep learning. Measurement of right heart structures from cardiovascular MRI using deep learning. In all panels, the PA is colored turquoise, the RV is colored red and the RA is colored yellow. The magnetic resonance images in this figure are reproduced by kind permission of UK Biobank. **a**, Graphical depictions of the right heart structures in a cutaway view of the heart. The art in this panel is derived from Servier Medical Art (licensed under creative commons by attribution, CC-BY-3.0). **b**, Cardiovascular MRI. SAX, short axis view; 4ch, four-chamber long axis view. The RV is visible in the SAX and 4ch views, the RA in the 4ch view and the PA in the basal SAX view. **c**, The raw images are fed into the trained deep learning model, producing pixel-by-pixel output (here, colorized and laid on top of the raw images). **d**, The deep learning models are applied to all images, allowing measurement of the right heart structures. **e**, The right ventricular surface is reconstructed by combining data from SAX and 4ch images (Methods), allowing a volumetric measurement.

quality control results are detailed in the Supplementary Note. Several loci were shared by multiple traits; counting each locus only once, we identified 130 independent loci associated with one or more right heart traits at a commonly used significance threshold of $P<5\times10^{-8}$ (Supplementary Table 7). Of these 130 loci, 71 were associated with at least two right heart traits, and one locus (near *WNT9B*/*GOSR2*/*MYL4*) was associated with 14 right heart phenotypes.

We conducted within-sample GWAS analyses of left ventricular and aortic traits, allowing us to identify that 58 of the 130 right heart loci were also associated at $P<5\times10^{-8}$ with left heart phenotypes, while 72 were right heart-specific (Table 2). Of the 72 right heart-specific loci, 12 came to significance only after adjusting the right heart traits for their left heart counterparts (Supplementary Fig. 10). Of the 72 loci, 48 were associated with dimensionless right heart phenotypes (for example, RVEF and the RVEDV/LVEDV ratio) or right heart phenotypes that accounted for BSA (Supplementary Table 8), while 24 loci were significant only before accounting for body size, no longer remaining significant after BSA-indexing (Supplementary Table 9). In gene set enrichment analyses[38,39], the 48 loci that remained significant after accounting for body size were enriched for genes involved in cardiac proliferation, chamber development and septum morphogenesis (Supplementary Table 10).

All lead SNPs associated at $P<5\times10^{-8}$ with any left or right heart phenotype in this analysis, after clumping within each GWAS to remove SNPs in linkage disequilibrium (LD) ($r^2>0.001$), are reported in Supplementary Table 7, where they are assigned a study-wide locus identifier to facilitate comparison between phenotypes. Those SNPs that are within 500 kb of one another are considered to be at the same locus and assigned the same study-wide identifier, and the strongest associated SNP at that locus is termed the lead SNP.

Gene-based analyses, including a transcriptome-wide association study (TWAS), exome sequencing-based rare variant analysis, and OpenTargets gene set enrichment analyses, are detailed in the Supplementary Note.

Right ventricular loci. Among the right ventricular phenotypes, RVESV was linked with the greatest number of loci (20). Of these 20 loci, 7 were also associated with the left heart counterpart (LVESV) of the RVESV at genome-wide significance. The effects of each SNP on right and left ventricular phenotypes are depicted in Fig. 5.

The strongest common variant association with RVESV was from a variant near *BAG3*; this same variant (rs72840788) was also the SNP with the strongest association with LVESV, with concordant effects. The rs72840788 variant is in near perfect LD with rs2234962, which leads to the missense change p.Cys151Arg in the BAG3 protein (Supplementary Fig. 11).

Two SNPs at the *TTN* locus had association $P<5\times10^{-8}$ with RVESV and were in linkage equilibrium ($r^2=0.001$) with one another: rs955738 ($P=4.4\times10^{-11}$) and rs2562845 ($P=4.2\times10^{-8}$). Whereas both SNPs were also associated with LVESV, the pattern of association strength was reversed when compared with the RVESV (rs2562845 was more strongly associated with LVESV than rs955738; Supplementary Fig. 12). It is possible that this distinction between primary association signals in the two ventricles is associated with differences in the regulation of *TTN* between the first (LV) and second (RV) heart fields, but establishing this will require additional investigation.

Among loci that were significantly associated with RVESV but not LVESV, some, like the *GATA4*/*CTSB*/*FDFT1* locus on chromosome 8, had a cluster of subthreshold SNPs for LVESV. At this locus, the RVESV lead SNP (rs34015932, $P=3.4\times10^{-8}$) was correlated only weakly ($r^2=0.16$) with the strongest LVESV-associated SNP near the locus (rs750190198, $P=1.1\times10^{-6}$), also suggesting allelic heterogeneity (Supplementary Fig. 13). Other loci, such as that of *OBSCN*—encoding obscurin, a giant sarcomeric protein in the same family as titin—seemed to be right-ventricle specific, showing very little evidence of association with left ventricular phenotypes (Supplementary Fig. 14).

Finally, some loci achieved $P<5\times10^{-8}$ only after adjustment of the right ventricular phenotype for its left ventricular counterpart (Supplementary Fig. 15). These include variants near *ADCY5*, which encodes the main isoform of adenylyl cyclase in the heart; pathogenic variation in this gene has previously been associated with heart failure[40].

Pulmonary artery and pulmonary root loci. Counting SNPs once for each associated trait, there were 172 trait-locus pairs associated with proximal PA diameter or pulmonary root diameter. A total of

82 distinct genomic loci were associated with at least one PA or pulmonary root phenotype. Of these, 40 were exclusive to these tissues and were not associated with phenotypes from the other right or left heart compartments. Whereas 7 loci were shared by both the PA and pulmonary root, 16 were exclusive to PA diameter measurements, and 17 were exclusive to pulmonary root measurements. No loci were significantly associated with PA strain. Of 28 lead SNPs for PA diameter that were identified in the Framingham Heart Study (FHS), 25 had concordant effect direction (binomial test two-tailed $P = 2.7 \times 10^{-5}$; Supplementary Table 11 and Supplementary Fig. 16). This external replication is detailed in the Supplementary Note.

Several loci had putative connections to vascular tone. A locus associated with both pulmonary root and PA diameter, but via distinct SNPs (r^2 between artery-associated rs79013608 and root-associated rs10770612 = 0.006) was found in an intergenic region whose nearest protein-coding gene is *PDE3A*. The protein product of this gene is inhibited by milrinone and cilostazol, which are in clinical use and have been shown in humans to reduce PA pressure[41,42]. A locus associated exclusively with PA diameter was tagged by a lead SNP intronic to *KCNMA1*, which encodes the channel-forming alpha subunit of the BK_{Ca} or the large conductance calcium- and voltage-activated potassium channels[43]. In a rat model, activation of endothelial BK_{Ca} channels in pulmonary endothelial cells was previously reported to cause pulmonary vasodilation[44].

Some of the loci that were associated predominantly with the pulmonary root rather than the PA had previously been associated with aortic root or aortic valve phenotypes. For example, a pulmonary root-specific locus near *CFDP1* from our study has previously been linked to aortic valve stenosis[45]. Another locus near *GOSR2* has an association with the pulmonary root that is 35 orders of magnitude stronger than its association with the PA; it has been linked previously to aortic valve area[46]. The *PALMD* locus has been associated previously with the diameter of the aortic root and with aortic valve stenosis in humans[47,48]. The SNPs at the *PALMD* locus identified in our analysis were in tight LD with those from Wild et al. ($r^2 = 0.96$-1.0)[49]. In fact, of the 12 aortic root-associated loci in Wild et al. achieving $P < 5 \times 10^{-8}$ in their discovery analysis, 7 were associated significantly with the pulmonary root in our present analysis, including loci near *CDFP1*, *CEP120* (previously *CCDC100*), *GOSR2*, *PALMD*, *HMGA2*, *PDE3A* and the *KCNRG*/*DLEU1* locus.

Right atrial loci. There were 42 trait-locus pairs associated with right atrial size and function. Accounting for multiple phenotypes having an association at the same locus, 20 genomic loci were associated with at least one right atrial phenotype. Of these, five were identified only in association with right atrial phenotypes and not other compartments: the lead SNPs at these loci were nearest to *HDGLF1*, *CCNL1*, *NRG1*, *FOXP1* and *ZFPM2*. The latter three are notable for their established roles in cardiovascular development and disease.

The protein product of *ZFPM2* interacts with GATA transcription factors, particularly GATA4, and plays a role in cardiac development[50,51]. Variants in *ZFPM2* have previously been linked to congenital heart defects[52–54]. In mice, Foxp1 has been shown to play a role in cardiac morphogenesis and, in humans, *FOXP1* variants have been linked to congenital heart defects[55–57]. Finally, *NRG1* encodes neuregulin-1, which participates in signaling through receptor tyrosine kinases and ErbB signaling in particular[58–60]. Clinical trials are ongoing to assess the effects of recombinant neuregulin on heart failure[61]. The rs112852637-T allele is associated with reduced right atrial area during atrial systole; reduced atrial area is associated inversely with arrhythmias and heart failure (Fig. 2 and Supplementary Table 3). This same allele is directionally associated with increased *NRG1* expression in the right atrial appendage, although this expression signal is not statistically significant in GTEx v.8 (ref. [62]).

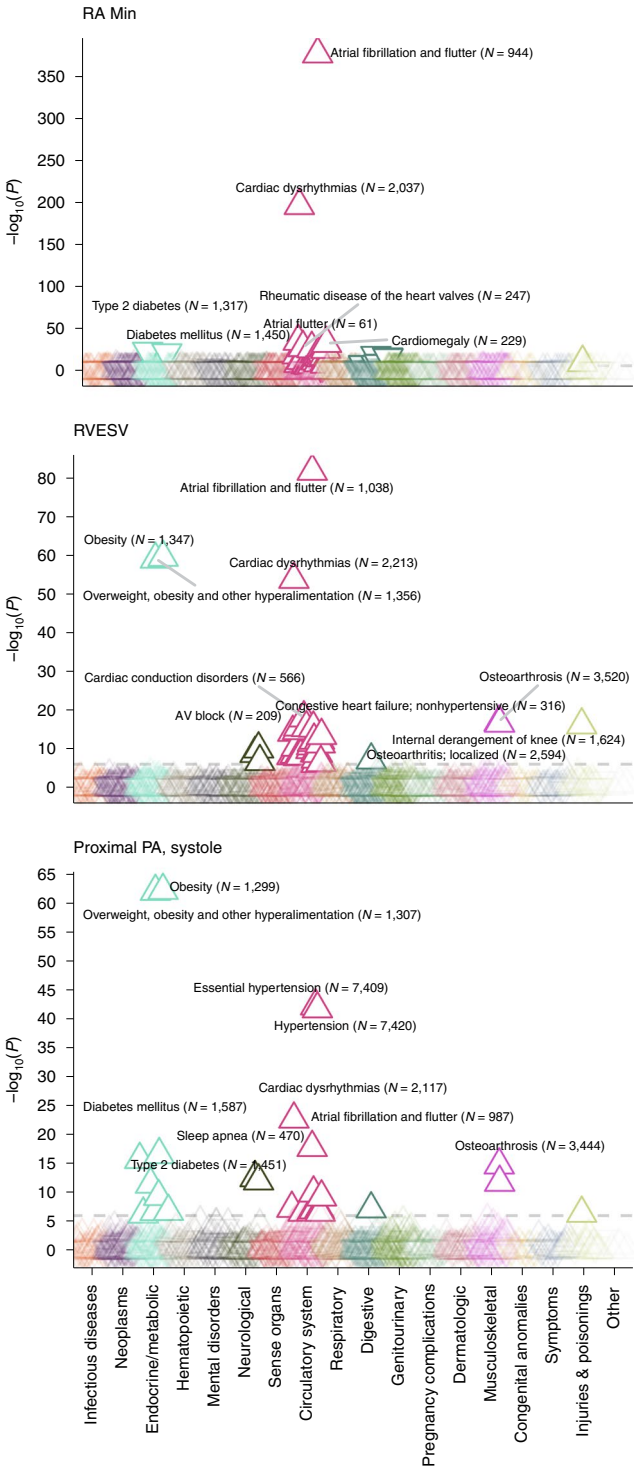

Fig. 2 | Right heart structures are associated with PheCode-based disease definitions. PheCode-based disease labels (*x* axis) are plotted against a transformation of their association *P* value (*y* axis) with three right heart phenotypes: minimum right atrial area, RVESV and proximal PA diameter. The values are derived from a linear model that associates the presence or absence of a PheCode-based disease with the right heart measurement, after adjustment for anthropometric covariates and genetic principal components. The direction of the arrow indicates whether the presence of the disease is associated with an increase (upward arrow) or a decrease (downward arrow) in the right heart measurement. The color indicates the disease grouping (as labeled on the *x* axis). All values are available in Supplementary Table 3. AV, atrioventricular.

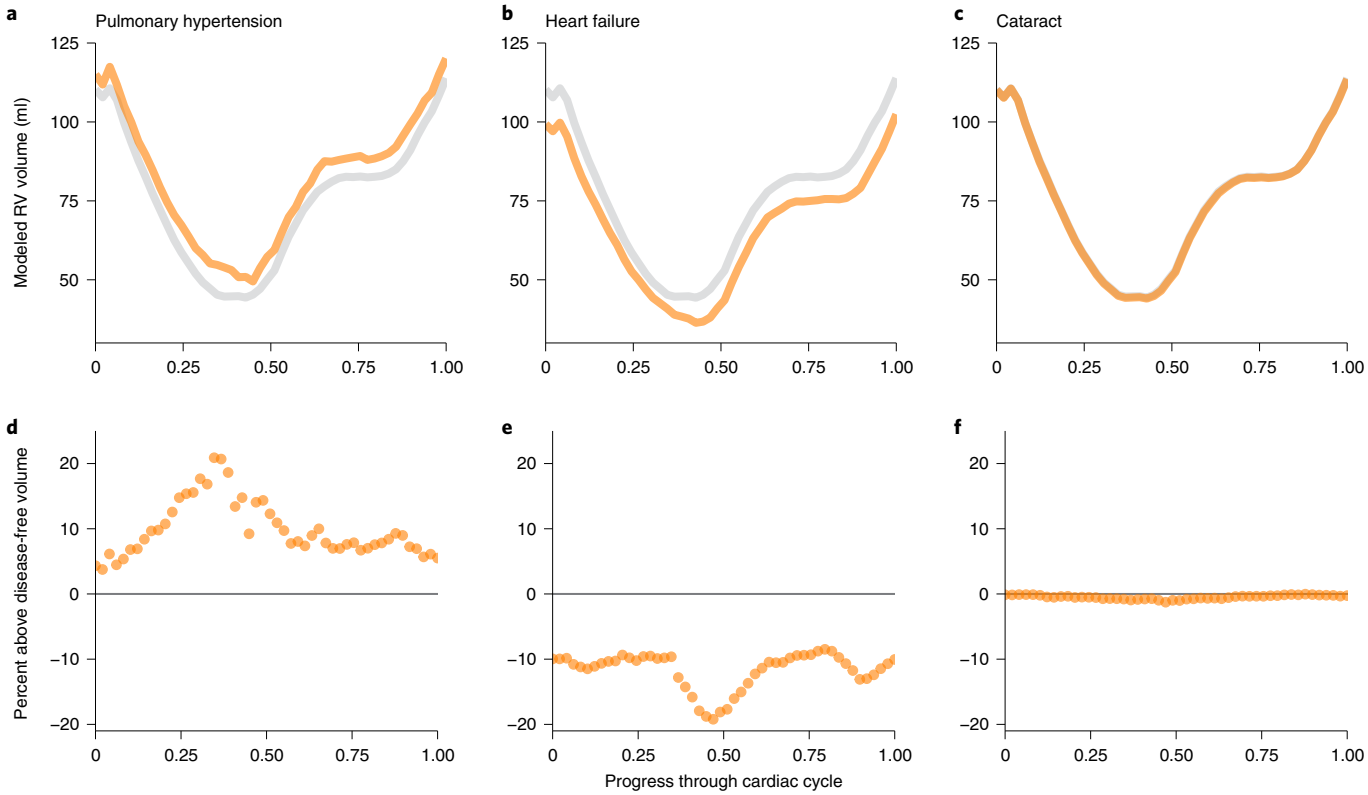

Fig. 3 | Alterations in right ventricular volume with prevalent disease. Disease diagnoses that occur before the date of MRI are linked with distinct changes in the volume of the RV throughout the cardiac cycle. For all panels, the *x* axis represents fractions of a cardiac cycle (divided evenly into 50 components, starting at end-diastole). **a**–**c**, The *y* axis represents volume. Values are generated with a linear model for each time point accounting for the left ventricular volume at that time point, as well as clinical covariates; gray line, population without disease; orange line, population with disease. In the UK Biobank, participants with pulmonary hypertension (**a**) have elevated right ventricular volume throughout the cardiac cycle, even after accounting for left ventricular volume. Those with heart failure (**b**) predominantly have elevated left ventricular volume, with relative sparing of their right ventricular volume (see Supplementary Fig. 4 for right ventricular volume without adjustment for left ventricular volume). Cataract (**c**) is used as a control to demonstrate little association between a noncardiovascular disease and RV volume. **d**–**f**, For pulmonary hypertension (**d**), heart failure (**e**) and cataract (**f**), at each time point the right ventricular volume of individuals with disease is subtracted from the volume without disease and divided by the volume without disease. This represents the percentage above or below the disease-free right ventricular volume for those with disease.

As a sensitivity analysis, we also assessed right atrial volumes. The GWAS results from those analyses are reported in Supplementary Table 12.

Right heart polygenic score analyses and external validation. We used PRScs-auto to compute around 1.1 million-SNP polygenic scores for RVEDV, RVESV and RVEF[63], finding the RVEF score to be correlated most strongly with dilated cardiomyopathy (DCM; Supplementary Table 13). There were 603 DCM events and 359,296 nonevents among UK Biobank participants unrelated to the MRI cohort; hazard ratio (HR) 1.33 per s.d. decrease; $P = 7.1 \times 10^{-13}$. Even after adjustment for a 1.1 million SNP polygenic score derived from the previously reported BSA-indexed left ventricular end systolic volume (LVESVi) GWAS, the RVEF score remained significantly associated with DCM (HR 1.21 per s.d. decrease; $P = 1.2 \times 10^{-5}$; Fig. 6). These findings were replicated, with attenuation, in the Mass General Brigham (MGB) Biobank and BioBank Japan (BBJ; Supplementary Note)[64–66].

We performed the same PRScs-auto procedure to generate 1.1 million SNP scores for the PA phenotypes. Of these, only the score for the proximal PA diameter in systole was associated with pulmonary hypertension in the UK Biobank (1,405 cases and 371,985 controls; HR 1.09 per s.d.; $P = 2.2 \times 10^{-3}$; Supplementary Table 13). This association remained significant in MGB, but not in BBJ (Supplementary Note). This polygenic score explained approximately 6.5% of the heritability of PA diameter based on an external analysis in FHS (Supplementary Note).

A PRScs-auto polygenic score for RA FAC was weakly inversely associated with the risk of atrial fibrillation or flutter (for 13,928 events and 353,311 nonevents; HR 0.98 per s.d.; $P = 1.9 \times 10^{-2}$). The evidence was slightly stronger when considering only atrial flutter as the outcome of interest (841 atrial flutter events and 372,565 nonevents; HR 0.91 per s.d.; $P = 4.9 \times 10^{-3}$).

Limitations. This study is subject to limitations. The study population is largely of European ancestries, similar to the remainder of UK Biobank, limiting generalizability of the findings to other populations. In future work, genetic analyses of these phenotypes in people of globally diverse ancestries will be important. Future work will be required to understand whether polygenic scores are associated with disease progression. The transcriptional data used in the TWAS came from left-sided structures (aortic gene expression for the PA and left ventricular gene expression for the RV), which may not capture right-sided expression patterns. The disease gene enrichment analyses account for local genomic context and gene density, but not for other features such as chromatin interactions. We focused on the genes nearest to the strongest association signals; future work will be required to determine the causal factors driving each association. OpenTargets scores are determined algorithmically and can change between versions. Because we used

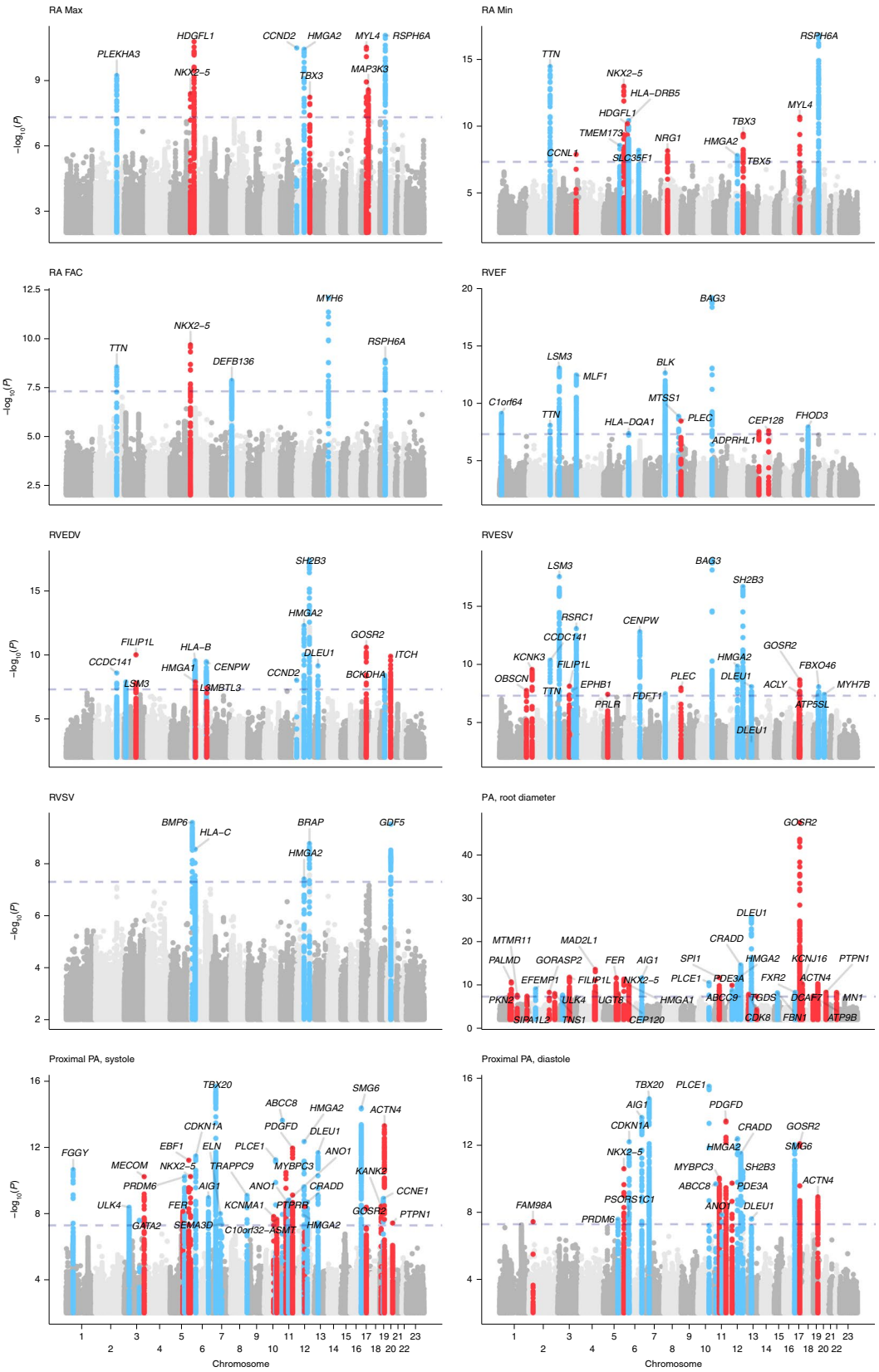

Fig. 4 | Manhattan plots of right heart traits. Manhattan plots show the chromosomal position (*x* axis) and the strength of association ($-\log_{10}$ of the *P* value, *y* axis) for all non-BSA-indexed phenotypes. The X chromosome is represented as 'Chromosome 23.' Loci that contain SNPs with $P < 5 \times 10^{-8}$ were labeled with the name of the nearest gene; genes may be represented multiple times for the same trait when multiple variants at the same locus are in linkage equilibrium with one another ($r^2 < 0.001$). Loci were colored blue if they were also associated with left heart phenotypes with $P < 5 \times 10^{-8}$, and red otherwise. SNPs with $P > 0.01$ are not plotted. Manhattan plots by compartment are available in Supplementary Fig. 7 (RA), Supplementary Fig. 8 (RV) and Supplementary Fig. 9 (pulmonary root and PA).

Table 2 | Loci specific to the right atrium and right ventricle

Trait	CHR	BP	SNP	Effect allele	Other allele	EAF	BETA	s.e.	*P* value	Nearest gene
RVEDV	3	99779984	rs57848867	A	T	0.526	−0.034	0.0053	9.90×10^{-11}	*FILIP1L*
RVEDV	6	34205465	rs202228093	G	GGAGCCC	0.106	0.05	0.0087	1.30×10^{-8}	*HMGA1*
RVEDV	6	130349119	rs6569648	C	T	0.238	0.034	0.0062	3.80×10^{-8}	*L3MBTL3*
RVEDV	17	45128762	rs1056064	T	C	0.833	−0.047	0.0071	2.60×10^{-11}	*GOSR2*
RVEDV	20	32987687	rs62212171	T	C	0.859	0.05	0.0076	1.30×10^{-10}	*ITCH*
RVESV	1	228556788	rs3738685	C	T	0.626	−0.031	0.0056	1.80×10^{-8}	*OBSCN*
RVESV	2	26922062	rs1314982	G	A	0.261	0.039	0.0062	2.80×10^{-10}	*KCNK3*
RVESV	3	99779984	rs57848867	A	T	0.526	−0.031	0.0055	7.70×10^{-9}	*FILIP1L*
RVESV	5	35191701	rs67209755	T	C	0.813	0.038	0.007	3.80×10^{-8}	*PRLR*
RVESV	8	145018354	rs11786896	C	T	0.951	0.071	0.0126	1.10×10^{-8}	*PLEC*
RVESV	17	40023617	rs781797066	T	TA	0.826	−0.041	0.0073	3.10×10^{-8}	*ACLY*
RVESV	17	45013271	rs17608766	T	C	0.858	−0.046	0.0077	2.20×10^{-9}	*GOSR2*
RVEF	8	145018354	rs11786896	C	T	0.951	−0.095	0.0159	3.60×10^{-9}	*PLEC*
RVEF	13	114075109	rs76382172	G	C	0.964	−0.101	0.0185	3.10×10^{-8}	*ADPRHL1*
RVEF	14	81171138	rs34540535	T	C	0.958	0.098	0.0175	2.60×10^{-8}	*CEP128*
RA Max	5	172664163	rs6882776	G	A	0.712	−0.041	0.0071	4.20×10^{-9}	*NKX2-5*
RA Max	6	22613847	rs7757005	G	A	0.642	−0.046	0.0067	1.70×10^{-11}	*HDGFL1*
RA Max	12	115162091		GTGTGCCCC	G	0.623	0.04	0.0067	6.10×10^{-9}	*TBX3*
RA Max	17	45280802	rs117154502	T	G	0.94	−0.089	0.0134	3.10×10^{-11}	*MYL4*
RA Max	17	61772449		GA	G	0.636	−0.041	0.007	2.80×10^{-9}	*MAP3K3*
RA Min	3	156827227	rs11928162	C	T	0.53	−0.037	0.0065	1.40×10^{-8}	*CCNL1*
RA Min	5	172662024	rs2277923	T	C	0.703	−0.053	0.0071	1.10×10^{-13}	*NKX2-5*
RA Min	6	22613847	rs7757005	G	A	0.642	−0.045	0.0068	7.00×10^{-11}	*HDGFL1*
RA Min	8	32413240	rs112852637	T	C	0.529	−0.038	0.0065	7.60×10^{-9}	*NRG1*
RA Min	12	114835428	rs1895602	G	T	0.545	−0.037	0.0067	4.90×10^{-8}	*TBX5*
RA Min	12	115162091		GTGTGCCCC	G	0.623	0.043	0.0068	4.30×10^{-10}	*TBX3*
RA Min	17	45280802	rs117154502	T	G	0.94	−0.091	0.0136	2.30×10^{-11}	*MYL4*
RA FAC	5	172644017	rs12652726	C	T	0.856	0.066	0.0105	2.10×10^{-10}	*NKX2-5*
RVEDV Indexed	3	99779984	rs57848867	A	T	0.525	−0.046	0.0063	3.20×10^{-13}	*FILIP1L*
RVEDV Indexed	10	30332445	rs4749523	A	G	0.634	0.037	0.0066	3.60×10^{-8}	*KIAA1462*
RVEDV Indexed	11	57771538	rs10526240	T	A	0.704	0.044	0.007	2.50×10^{-10}	*OR9Q1*
RVEDV Indexed	17	45013271	rs17608766	T	C	0.858	−0.064	0.0089	6.30×10^{-13}	*GOSR2*
RVESV Indexed	1	228556788	rs3738685	C	T	0.626	−0.038	0.0064	7.50×10^{-10}	*OBSCN*
RVESV Indexed	2	26922062	rs1314982	G	A	0.26	0.046	0.0071	2.60×10^{-11}	*KCNK3*
RVESV Indexed	3	99779984	rs57848867	A	T	0.525	−0.038	0.0062	1.50×10^{-9}	*FILIP1L*
RVESV Indexed	4	169847115		TA	T	0.2	0.044	0.0079	1.70×10^{-8}	*PALLD*
RVESV Indexed	8	9287587	rs28549922	G	A	0.861	−0.05	0.0089	4.20×10^{-9}	*TNKS*
RVESV Indexed	8	145018354	rs11786896	C	T	0.951	0.083	0.0144	7.00×10^{-9}	*PLEC*
RVESV Indexed	14	81171138	rs34540535	T	C	0.958	−0.095	0.0158	8.40×10^{-10}	*CEP128*
RVESV Indexed	17	45013271	rs17608766	T	C	0.858	−0.056	0.0088	7.40×10^{-11}	*GOSR2*
RVSV Indexed	3	99779984	rs57848867	A	T	0.525	−0.039	0.007	2.40×10^{-8}	*FILIP1L*
RVSV Indexed	11	57771538	rs10526240	T	A	0.704	0.045	0.0077	8.10×10^{-9}	*OR9Q1*
RA Max Indexed	3	71599571	rs7640614	C	G	0.606	−0.044	0.0075	7.40×10^{-9}	*FOXP1*
RA Max Indexed	8	32413240	rs112852637	T	C	0.529	−0.042	0.0074	1.10×10^{-8}	*NRG1*
RA Max Indexed	8	106379363	rs201748964	T	G	0.691	−0.043	0.0079	4.20×10^{-8}	*ZFPM2*
RA Max Indexed	12	115162091		GTGTGCCCC	G	0.623	0.045	0.0077	5.20×10^{-9}	*TBX3*
RA Max Indexed	17	45280802	rs117154502	T	G	0.94	−0.092	0.0154	3.10×10^{-9}	*MYL4*
RA Min Indexed	5	172664163	rs6882776	G	A	0.712	−0.052	0.0081	1.50×10^{-10}	*NKX2-5*

Continued

Table 2 | Loci specific to the right atrium and right ventricle (continued)

Trait	CHR	BP	SNP	Effect allele	Other allele	EAF	BETA	s.e.	*P* value	Nearest gene
RA Min Indexed	8	32413240	rs112852637	T	C	0.529	−0.045	0.0074	6.80×10^{-10}	*NRG1*
RA Min Indexed	12	115164024	rs11067264	G	A	0.623	0.05	0.0076	6.60×10^{-11}	*TBX3*
RA Min Indexed	17	45280802	rs117154502	T	G	0.94	−0.094	0.0153	8.60×10^{-10}	*MYL4*
RVEDV/LVEDV Ratio	2	42145432	rs2374381	T	C	0.7	0.044	0.0077	6.20×10^{-9}	*C2orf91*
RVEDV/LVEDV Ratio	6	126068914	rs1935983	C	T	0.391	−0.048	0.0072	3.80×10^{-11}	*HEY2*
RVEDV/LVEDV Ratio	7	136636260	rs112206296	A	C	0.985	0.178	0.0299	4.30×10^{-9}	*CHRM2*
RVEDV/LVEDV Ratio	9	73049120	rs61634638	G	GT	0.41	−0.041	0.0072	1.30×10^{-8}	*KLF9*
RVEDV/LVEDV Ratio	12	123639539	rs67657805	T	TA	0.238	−0.049	0.0087	1.50×10^{-8}	*MPHOSPH9*
RVESV/LVESV Ratio	3	123105119	rs62262391	C	T	0.777	−0.053	0.0086	7.60×10^{-10}	*ADCY5*
RVESV/LVESV Ratio	6	73906746	rs10943078	A	T	0.757	−0.047	0.0083	1.50×10^{-8}	*KCNQ5*
RVESV/LVESV Ratio	6	126090377	rs9388451	T	C	0.486	−0.04	0.0072	4.10×10^{-8}	*HEY2*
RVESV/LVESV Ratio	10	76089763		TA	T	0.263	−0.046	0.0083	2.60×10^{-8}	*ADK*
RVESV/LVESV Ratio	12	123493123	rs12820906	A	G	0.755	0.05	0.0083	1.80×10^{-9}	*PITPNM2*
RVEF/LVEF Ratio	3	123110581	rs55968914	C	G	0.777	0.057	0.0088	1.40×10^{-10}	*ADCY5*

Shown are clumped SNPs with BOLT-LMM $P<5\times10^{-8}$ from the right atrial and right ventricular GWAS, excluding those that were also found in left ventricular or aortic GWAS within the same participants. PA and pulmonary root loci are too numerous to represent here; all right and left-heart loci with $P<5\times10^{-8}$ can be found in Supplementary Table 7. For ratio phenotypes (for example, 'RVEDV/LVEDV,' which represents the RVEDV-to-LVEDV ratio), the SNPs listed here must additionally not be found within 500 kb of SNPs from a nonratio phenotype. When multiple SNPs with $P<5\times10^{-8}$ are found within 500 kb of one another and are in linkage equilibrium ($r^2<0.001$), each independent SNP is displayed; an example is at the *TBX5/TBX3* locus for the 'RA Min' phenotype. In the Trait column, suffix -S represents 'systole,' -D represents 'diastole,' and Idx represents 'indexed to body surface area'. CHR, chromosome; BP, GRCh37 position; SNP, single nucleotide polymorphism (where a dbSNP ID was not available, this field was left empty because the SNP is uniquely identified by its position and alleles); EAF, effect allele frequency; BETA, effect size; s.e., standard error of effect size; *P* value, BOLT-LMM *P* value.

the hospital-based *International Classification of Diseases*, tenth revision (ICD-10) and procedural codes to identify individuals with disease, our study lacks an ARVC-specific analysis (which does not have a unique ICD-10 code), and our disease definitions are susceptible to misclassification. We describe technical limitations related to MRI acquisition and deep learning in the Supplementary Note.

Discussion

We produced measurements of the right heart, including the RA, RV and PA, analyzed their relationships with their left heart counterparts and with cardiovascular diseases, and identified 130 distinct genetic loci that were associated with these right heart measurements. We drew several conclusions from these findings.

First, right heart phenotypes, including structural and functional measurements of the RA, RV and PA, are heritable. While they share strong epidemiological and genetic correlation with the corresponding left heart structures, our findings of partial genetic correlation and distinct genome-wide significant loci also imply distinct drivers of variation between right and left heart structures. Of the 72 right heart-specific loci, 48 remained significant after accounting for the corresponding left heart structure or overall body size via BSA-indexing (Supplementary Table 8) and were associated with dozens of gene sets involved in cardiac morphogenesis and cardiomyocyte proliferation (Supplementary Table 10). A total of 12 loci achieved significance in neither left nor right heart GWAS in isolation, but instead only after indexing the right heart phenotype for its left heart counterpart (Supplementary Fig. 10). Developing a better understanding of these distinct drivers of right and left heart structure may ultimately permit more targeted therapies for RV-predominant heart failure syndromes and primary cardiomyopathies such as ARVC.

Second, we found that the GWAS loci were enriched for genes associated with developmental diseases. In addition to the *GATA4*, *ZFPM2*, *FOXP1* and *NRG1* loci addressed above, several others were notable for connections to cardiovascular development. Right heart structures were associated with SNPs near *NKX2-5*, which plays a key role in maintaining the progenitor pool of cells of the secondary heart field, resulting in outflow tract defects in people

Fig. 5 | Right heart loci. Right heart loci are shown grouped by trait. Where a paired left-heart phenotype is available, the effect size and *P* value for the same SNP are shown next to its corresponding right heart trait. Each grid region represents the lead SNP (sorted in chromosomal order and tagged by its nearest gene, labeled on the *y* axis) for each trait (*x* axis). The effect magnitude (Beta) is represented with shades of orange (increase) and blue (decrease), and the effect direction is oriented with respect to the minor allele within the study population. Black boxes within a grid region indicate that the association between the SNP and the trait has BOLT-LMM $P<5\times10^{-8}$; those with a smaller gray box indicate BOLT-LMM $P<5\times10^{-6}$. Exact effect sizes and *P* values are provided in Supplementary Table 7 for traits with BOLT-LMM $P<5\times10^{-8}$, and in the publicly available summary statistics where BOLT-LMM $P\geq5\times10^{-8}$. 'PA/Ao' is the ratio of the PA diameter to the ascending aortic diameter. 'Indexed' traits have been divided by body surface area. Genes may be represented multiple times for the same trait when multiple variants at the same locus are in linkage equilibrium with one another ($r^2<0.001$).

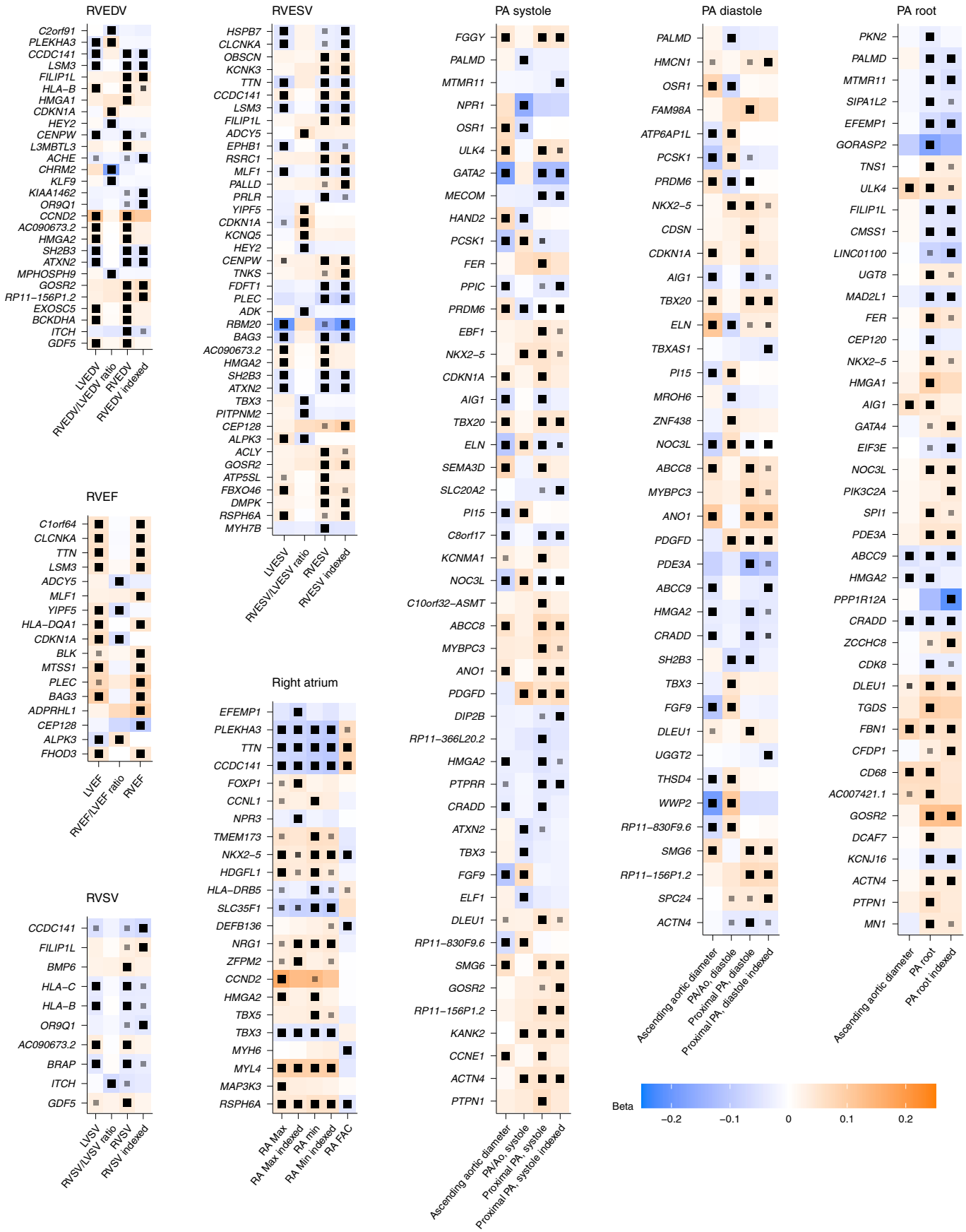
RVEDV
C2orf91
PLEKHA3
CCDC141
LSM3
FILIP1L
HLA–B
HMGA1
CDKN1A
HEY2
CENPW
L3MBTL3
ACHE
CHRM2
KLF9
KIAA1462
OR9Q1
CCND2
AC090673.2
HMGA2
SH2B3
ATXN2
MPHOSPH9
GOSR2
RP11–156P1.2
EXOSC5
BCKDHA
ITCH
GDF5
LVEDV
RVEDV/LVEDV ratio
RVEDV
RVEDV indexed
RVESV
HSPB7
CLCNKA
OBSCN
KCNK3
TTN
CCDC141
LSM3
FILIP1L
ADCY5
EPHB1
RSRC1
MLF1
PALLD
PRLR
YIPF5
CDKN1A
KCNQ5
HEY2
CENPW
TNKS
FDFT1
PLEC
ADK
RBM20
BAG3
AC090673.2
HMGA2
SH2B3
ATXN2
TBX3
PITPNM2
CEP128
ALPK3
ACLY
GOSR2
ATP5SL
FBXO46
DMPK
RSPH6A
MYH7B
LVESV
RVESV/LVESV ratio
RVESV
RVESV indexed
PA systole
FGGY
PALMD
MTMR11
NPR1
OSR1
ULK4
GATA2
MECOM
HAND2
PCSK1
FER
PPIC
PRDM6
EBF1
NKX2–5
CDKN1A
AIG1
TBX20
ELN
SEMA3D
SLC20A2
PI15
C8orf17
KCNMA1
NOC3L
C10orf32–ASMT
ABCC8
MYBPC3
ANO1
PDGFD
DIP2B
RP11–366L20.2
HMGA2
PTPRR
CRADD
ATXN2
TBX3
FGF9
ELF1
DLEU1
RP11–830F9.6
SMG6
GOSR2
RP11–156P1.2
KANK2
CCNE1
ACTN4
PTPN1
Ascending aortic diameter
PA/Ao, systole
Proximal PA, systole
Proximal PA, systole indexed
PA diastole
PALMD
HMCN1
OSR1
FAM98A
ATP6AP1L
PCSK1
PRDM6
NKX2–5
CDSN
CDKN1A
AIG1
TBX20
ELN
TBXAS1
PI15
MROH6
ZNF438
NOC3L
ABCC8
MYBPC3
ANO1
PDGFD
PDE3A
ABCC9
HMGA2
CRADD
SH2B3
TBX3
FGF9
DLEU1
UGGT2
THSD4
WWP2
RP11–830F9.6
SMG6
RP11–156P1.2
SPC24
ACTN4
Ascending aortic diameter
PA/Ao, diastole
Proximal PA, diastole
Proximal PA, diastole indexed
PA root
PKN2
PALMD
MTMR11
SIPA1L2
EFEMP1
GORASP2
TNS1
ULK4
FILIP1L
CMSS1
LINC01100
UGT8
MAD2L1
FER
CEP120
NKX2–5
HMGA1
AIG1
GATA4
EIF3E
NOC3L
PIK3C2A
SPI1
PDE3A
ABCC9
HMGA2
PPP1R12A
CRADD
ZCCHC8
CDK8
DLEU1
TGDS
FBN1
CFDP1
CD68
AC007421.1
GOSR2
DCAF7
KCNJ16
ACTN4
PTPN1
MN1
Ascending aortic diameter
PA root
PA root indexed
RVEF
C1orf64
CLCNKA
TTN
LSM3
ADCY5
MLF1
YIPF5
HLA–DQA1
CDKN1A
BLK
MTSS1
PLEC
BAG3
ADPRHL1
CEP128
ALPK3
FHOD3
LVEF
RVEF/LVEF ratio
RVEF
Right atrium
EFEMP1
PLEKHA3
TTN
CCDC141
FOXP1
CCNL1
NPR3
TMEM173
NKX2–5
HDGFL1
HLA–DRB5
SLC35F1
DEFB136
NRG1
ZFPM2
CCND2
HMGA2
TBX5
TBX3
MYH6
MYL4
MAP3K3
RSPH6A
RA Max
RA Max indexed
RA min
RA Min indexed
RA FAC
RVSV
CCDC141
FILIP1L
BMP6
HLA–C
HLA–B
OR9Q1
AC090673.2
BRAP
ITCH
GDF5
LVSV
RVSV/LVSV ratio
RVSV
RVSV indexed
Beta
−0.2
−0.1
0
0.1
0.2

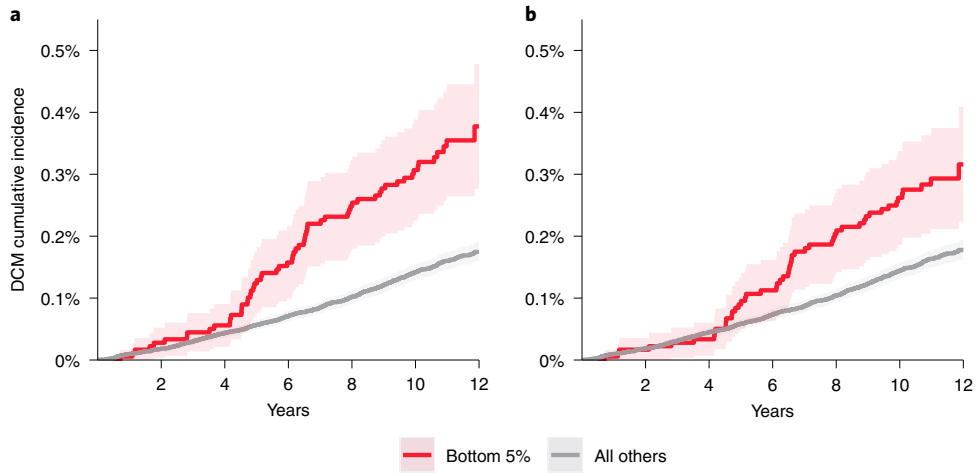

Fig. 6 | Cumulative incidence of dilated cardiomyopathy stratified by genetic prediction of RVEF. A total of 359,899 UK Biobank participants were unrelated within three degrees of the participants who underwent MRI. A total of 603 participants were diagnosed with DCM after enrollment. Those in the bottom 5% of genetically predicted RVEF are depicted in red and the remaining 95% are depicted in gray. The darker shades of red and gray represent the central estimate of the cumulative incidence (defined as 1 – the Kaplan-Meier survival estimate). The lighter shades of red and gray represent the respective 95% confidence intervals (based on the standard error). The *x* axis depicts years since enrollment in the UK Biobank; the *y* axis depicts cumulative incidence of dilated cardiomyopathy. **a**, Strata based on genetic prediction of RVEF. Those in the bottom 5% had an elevated risk of DCM (62 incident cases; Cox HR 2.2; $P = 7.6 \times 10^{-9}$). **b**, Strata based on genetic prediction of RVEF after residualization for genetic prediction of LVESVi. Those in the bottom 5% had an elevated risk of DCM (52 incident cases; Cox HR 1.8; $P = 5.4 \times 10^{-5}$). The Schoenfeld global *P* value for both models was 0.26, indicating no violation of the proportional hazards assumption.

with *NKX2-5* variants[5,67]; *MYL4*, which encodes atrial light chain 1, missense variants in which have been linked to familial atrial fibrillation[68] and *TBX3*, which controls the formation of the sinus node and loss of which leads to outflow tract malformations and septal defects[69–71]. The *TBX5*/*TBX3* locus also stands out because of the diversity of signals revealed in the data, with links to variation in RA, RV and PA (Supplementary Fig. 17). Two distinct signals drive the observed associations with right atrial size (rs1895602 near *TBX5*, and rs71447956/rs11067264 near *TBX3*). A third set of SNPs (rs4767282/rs10850409/rs35514224) is associated with the right-versus-left proportions of the ventricles and outflow tract. For example, at rs4767282, the C allele is associated with a slightly smaller RVESV and a slightly larger LVESV, achieving $P < 5 \times 10^{-8}$ only for the ratio of RVESV/LVESV. Given the proximity of these SNPs to *TBX5*, which plays a key role in atrial and ventricular septal placement[2,72,73], and *TBX3*, which is required for outflow tract development, and variants in which cause conotruncal defects[74,75], it is tempting to speculate that these signals may influence the left–right localization of the site of septation during development. Indeed, the right heart-specific loci are enriched for genes that play roles in cardiac septum development (near *NKX2-5*, *TBX3*, *TBX5*, *HEY2* and *ZFPM2*; Supplementary Table 10). We hypothesize that chamber-specific associations may be attributable to the different embryological origins of the right and left ventricles and their respective proximal conduction systems[76], the distinct afterload regimes they face or differences in physiological inputs during adult life. Future studies across the human lifespan will be helpful to answer this question.

Third, we observed links between cardiovascular disease and right ventricular measurements—as well as polygenic predictions of these measurements. Individuals with pre-existing diagnoses of pulmonary hypertension had enlarged right ventricular volumes throughout the cardiac cycle even after accounting for left ventricular volumes (Fig. 3). In UK Biobank participants, a polygenic predictor of RVEF was associated with incident dilated cardiomyopathy (Fig. 6). The RVEF polygenic score remained significantly associated with incident dilated cardiomyopathy even after accounting for a left ventricular polygenic score—implying a shared genetic basis for right ventricular dysfunction and dilated cardiomyopathy. These results were validated in external biobanks including MGB and BBJ—an external biobank of Japanese-ancestry participants. The role of right ventricular size and function as prognostic markers in individuals with dilated cardiomyopathy is well established[77]. Consistent with emerging clinical evidence, right ventricular structure and function are not merely of anthropometric interest, but instead represent endophenotypes for cardiomyopathy. Our findings suggest that earlier consideration of abnormalities of right ventricular function may afford the opportunity for earlier diagnosis of ensuing left ventricular dysfunction.

Fourth, we found epidemiological and genetic associations between proximal PA diameter and pulmonary hypertension. We produced a genome-wide polygenic prediction of PA diameter that was modestly associated with incident pulmonary hypertension in the UK Biobank; this finding was replicated externally in MGB. The genetic prediction of PA diameter accounted for approximately 6.5% of the heritability of PA diameter in an external cohort (FHS). A previous version of this score produced from only clumped, genome-wide significant SNPs did not find a significant association with pulmonary hypertension; we suspect that this discrepancy may be because variation in PA diameter is driven most strongly by genetic variants affecting size during development, and more weakly by the pressure of the pulmonary circuit—whose contributions may be mostly subgenome-wide significant at the current sample size. In future work, distinguishing the anatomical and developmental drivers of variation in cardiovascular structures from pathophysiological drivers may assist in the development of more clinically relevant polygenic scores[78]. As demonstrated by the lack of replication of the association between the PA score and pulmonary hypertension in BBJ, future ancestrally diverse discovery efforts will also be critical.

Finally, machine learning enables the derivation of complex traits in a manner that is scalable. This permits biobank-wide investigation of previously understudied human phenotypes, and promises to accelerate our understanding of cardiovascular disease.

Online content

Any methods, additional references, Nature Research reporting summaries, source data, extended data, supplementary information, acknowledgements, peer review information; details of author contributions and competing interests; and statements of data and code availability are available at https://doi.org/10.1038/s41588-022-01090-3.

Received: 5 February 2021; Accepted: 26 April 2022;
Published online: 13 June 2022

References

1. Olson, E. N. Gene regulatory networks in the evolution and development of the heart. *Science* **313**, 1922–1927 (2006).
2. Koshiba-Takeuchi, K. et al. Reptilian heart development and the molecular basis of cardiac chamber evolution. *Nature* **461**, 95–98 (2009).
3. Farmer, C. G. Evolution of the vertebrate cardio-pulmonary system. *Annu. Rev. Physiol.* **61**, 573–592 (1999).
4. Galli, D. et al. Atrial myocardium derives from the posterior region of the second heart field, which acquires left-right identity as Pitx2c is expressed. *Development* **135**, 1157–1167 (2008).
5. Meilhac, S. M. & Buckingham, M. E. The deployment of cell lineages that form the mammalian heart. *Nat. Rev. Cardiol.* **15**, 705–724 (2018).
6. Verzi, M. P., McCulley, D. J., De Val, S., Dodou, E. & Black, B. L. The right ventricle, outflow tract, and ventricular septum comprise a restricted expression domain within the secondary/anterior heart field. *Dev. Biol.* **287**, 134–145 (2005).
7. Zaffran, S., Kelly, R. G., Meilhac, S. M., Buckingham, M. E. & Brown, N. A. Right ventricular myocardium derives from the anterior heart field. *Circ. Res.* **95**, 261–268 (2004).
8. Jiang, X., Rowitch, D. H., Soriano, P., McMahon, A. P. & Sucov, H. M. Fate of the mammalian cardiac neural crest. *Development* **127**, 1607–1616 (2000).
9. Li, J., Chen, F. & Epstein, J. A. Neural crest expression of Cre recombinase directed by the proximal Pax3 promoter in transgenic mice. *Genesis* **26**, 162–164 (2000).
10. Lin, C.-J., Lin, C.-Y., Chen, C.-H., Zhou, B. & Chang, C.-P. Partitioning the heart: mechanisms of cardiac septation and valve development. *Development* **139**, 3277–3299 (2012).
11. Gotschy, A. et al. Right ventricular outflow tract dimensions in arrhythmogenic right ventricular cardiomyopathy/dysplasia-a multicentre study comparing echocardiography and cardiovascular magnetic resonance. *Eur. Heart J. Cardiovasc. Imaging* **19**, 516–523 (2018).
12. Marcus, F. I. et al. Diagnosis of arrhythmogenic right ventricular cardiomyopathy/dysplasia. *Circulation* **121**, 1533–1541 (2010).
13. McKoy, G. et al. Identification of a deletion in plakoglobin in arrhythmogenic right ventricular cardiomyopathy with palmoplantar keratoderma and woolly hair (Naxos disease). *Lancet* **355**, 2119–2124 (2000).
14. McNally, E., et al. Arrhythmogenic right ventricular cardiomyopathy. In: GeneReviews [Internet] Seattle, WA: University of Washington, Seattle, 1993–2002. 18 April 2005 (updated 25 May 2017).
15. Protonotarios, N. & Tsatsopoulou, A. Naxos disease: cardiocutaneous syndrome due to cell adhesion defect. *Orphanet J. Rare Dis.* **1**, 4 (2006).
16. Romero, J., Mejia-Lopez, E., Manrique, C. & Lucariello, R. Arrhythmogenic right ventricular cardiomyopathy (ARVC/D): a systematic literature review. *Clin Med Insights Cardiol* **7**, CMC.S10940 (2013).
17. Behr, E. R., Ben-Haim, Y., Ackerman, M. J., Krahn, A. D. & Wilde, A. A. M. Brugada syndrome and reduced right ventricular outflow tract conduction reserve: a final common pathway? *Eur. Heart J.* **42**, 1073–1081 (2021).
18. Ghio, S. et al. Independent and additive prognostic value of right ventricular systolic function and pulmonary artery pressure in patients with chronic heart failure. *J. Am. Coll. Cardiol.* **37**, 183–188 (2001).
19. Kjaergaard, J. et al. Right ventricular dysfunction as an independent predictor of short- and long-term mortality in patients with heart failure. *Eur. J. Heart Fail.* **9**, 610–616 (2007).
20. Melenovsky, V., Hwang, S.-J., Lin, G., Redfield, M. M. & Borlaug, B. A. Right heart dysfunction in heart failure with preserved ejection fraction. *Eur. Heart J.* **35**, 3452–3462 (2014).
21. Bai, W. et al. Automated cardiovascular magnetic resonance image analysis with fully convolutional networks. *J. Cardiovasc. Magn. Reson.* **20**, 65 (2018).
22. Bai, W. et al. A population-based phenome-wide association study of cardiac and aortic structure and function. *Nat. Med.* **26**, 1654–1662 (2020).
23. Petersen, S. E. et al. Imaging in population science: cardiovascular magnetic resonance in 100,000 participants of UK Biobank—rationale, challenges and approaches. *J. Cardiovasc. Magn. Reson.* **15**, 46 (2013).
24. Petersen, S. E. UK Biobank's cardiovascular magnetic resonance protocol. *J. Cardiovasc. Magn. Reson.* **18**, 8 (2016).
25. Sudlow, C. et al. UK biobank: an open access resource for identifying the causes of a wide range of complex diseases of middle and old age. *PLoS Med.* **12**, e1001779 (2015).
26. Howard, J. & Gugger, S. Fastai: a layered API for deep learning. *Information* **11**, 108 (2020).
27. Paszke, A. et al. PyTorch: an imperative style, high-performance deep learning library. Preprint at *arXiv* https://doi.org/10.48550/arXiv.1912.01703 (2019).
28. Deng, J. et al. ImageNet: a large-scale hierarchical image database. In *2009 IEEE Conference on Computer Vision and Pattern Recognition* 248–255 (IEEE, 2009). https://doi.org/10.1109/CVPR.2009.5206848
29. Krizhevsky, A., Sutskever, I. & Hinton, G. E. ImageNet classification with deep convolutional neural networks. *Commun. ACM* **60**, 84–90 (2017).
30. Ronneberger, O., Fischer, P. & Brox, T. U-Net: convolutional networks for biomedical image segmentation. Preprint at *arXiv* https://doi.org/10.48550/arXiv.1505.04597 (2015).
31. Dice, L. R. Measures of the amount of ecologic association between species. *Ecology* **26**, 297–302 (1945).
32. Sørensen, T. J. A method of establishing groups of equal amplitude in plant sociology based on similarity of species content and its application to analyses of the vegetation on Danish commons. *K. Dan. Vidensk. Selsk. Biol. Skr.* **5**, 1–34 (1948).
33. Pirruccello, J. P. et al. Deep learning enables genetic analysis of the human thoracic aorta. *Nat. Genet.* **54**, 40–51 (2022).
34. Edwards, P. D., Bull, R. K. & Coulden, R. CT measurement of main pulmonary artery diameter. *Br. J. Radiol.* **71**, 1018–1020 (1998).
35. Sanfilippo, A. J. et al. Atrial enlargement as a consequence of atrial fibrillation. A prospective echocardiographic study. *Circulation* **82**, 792–797 (1990).
36. Loh, P.-R. et al. Efficient Bayesian mixed-model analysis increases association power in large cohorts. *Nat. Genet.* **47**, 284–290 (2015).
37. Loh, P.-R., Kichaev, G., Gazal, S., Schoech, A. P. & Price, A. L. Mixed-model association for biobank-scale datasets. *Nat. Genet.* **50**, 906–908 (2018).
38. Liberzon, A. et al. Molecular signatures database (MSigDB) 3.0. *Bioinformatics* **27**, 1739–1740 (2011).
39. Subramanian, A. et al. Gene set enrichment analysis: a knowledge-based approach for interpreting genome-wide expression profiles. *Proc. Natl Acad. Sci. USA* **102**, 15545–15550 (2005).
40. Chen, Y.-Z. Autosomal dominant familial dyskinesia and facial myokymia: single exome sequencing identifies a mutation in adenylyl cyclase 5. *Arch. Neurol.* **69**, 630 (2012).
41. Givertz, M. M., Hare, J. M., Loh, E., Gauthier, D. F. & Colucci, W. S. Effect of bolus milrinone on hemodynamic variables and pulmonary vascular resistance in patients with severe left ventricular dysfunction: a rapid test for reversibility of pulmonary hypertension. *J. Am. Coll. Cardiol.* **28**, 1775–1780 (1996).
42. Sahin, M. et al. The effect of cilostazol on right heart function and pulmonary pressure. *Cardiovasc. Ther.* **31**, e88–e93 (2013).
43. Singh, H. et al. mitoBKCa is encoded by the *Kcnma1* gene, and a splicing sequence defines its mitochondrial location. *Proc. Natl Acad. Sci. USA* **110**, 10836–10841 (2013).
44. Vang, A., Mazer, J., Casserly, B. & Choudhary, G. Activation of endothelial BKCa channels causes pulmonary vasodilation. *Vascul. Pharmacol.* **53**, 122–129 (2010).
45. Helgadottir, A. et al. Genome-wide analysis yields new loci associating with aortic valve stenosis. *Nat. Commun.* **9**, 987 (2018).
46. Córdova-Palomera, A. et al. Cardiac imaging of aortic valve area from 34 287 UK Biobank participants reveals novel genetic associations and shared genetic comorbidity with multiple disease phenotypes. *Circ. Genom. Precis. Med.* **13**, e003014 (2020).
47. Thériault, S. et al. A transcriptome-wide association study identifies *PALMD* as a susceptibility gene for calcific aortic valve stenosis. *Nat. Commun.* **9**, 988 (2018).
48. Wild, P. S. et al. Large-scale genome-wide analysis identifies genetic variants associated with cardiac structure and function. *J. Clin. Invest.* **127**, 1798–1812 (2017).
49. Machiela, M. J. & Chanock, S. J. LDlink: a web-based application for exploring population-specific haplotype structure and linking correlated alleles of possible functional variants. *Bioinformatics* **31**, 3555–3557 (2015).
50. Lu, J. et al. FOG-2, a heart- and brain-enriched cofactor for GATA transcription factors. *Mol. Cell. Biol.* **19**, 4495–4502 (1999).
51. Svensson, E. C., Tufts, R. L., Polk, C. E. & Leiden, J. M. Molecular cloning of FOG-2: A modulator of transcription factor GATA-4 in cardiomyocytes. *Proc. Natl Acad. Sci. USA* **96**, 956–961 (1999).
52. D'Alessandro, L. C. A. et al. Exome sequencing identifies rare variants in multiple genes in atrioventricular septal defect. *Genet Med* **18**, 189–198 (2016).

53. Pu, T. et al. Identification of *ZFPM2* mutations in sporadic conotruncal heart defect patients. *Mol. Genet. Genomics* **293**, 217–223 (2018).
54. Qian, Y. et al. Multiple gene variations contributed to congenital heart disease via GATA family transcriptional regulation. *J. Transl. Med.* **15**, 69 (2017).
55. Chang, S.-W. et al. Genetic abnormalities in *FOXP1* are associated with congenital heart defects. *Hum. Mutat.* **34**, 1226–1230 (2013).
56. Lozano, R. et al. *FOXP1* syndrome: a review of the literature and practice parameters for medical assessment and monitoring. *J. Neurodev. Disord.* **13**, 18 (2021).
57. Wang, B. et al. Foxp1 regulates cardiac outflow tract, endocardial cushion morphogenesis and myocyte proliferation and maturation. *Development* **131**, 4477–4487 (2004).
58. Meyer, D. & Birchmeier, C. Multiple essential functions of neuregulin in development. *Nature* **378**, 386–390 (1995).
59. Rentschler, S. et al. Neuregulin-1 promotes formation of the murine cardiac conduction system. *Proc. Natl Acad. Sci. USA* **99**, 10464–10469 (2002).
60. Rupert, C. E. & Coulombe, K. L. The roles of Neuregulin-1 in cardiac development, homeostasis, and disease. *Biomark Insights* **10**, 1–9 (2015).
61. *Evaluate the effect of injectable neucardin on the cardiac function of subjects with chronic systolic heart failure* (Zensun Sci. & Tech. Co., Ltd, accessed June 24, 2021); https://clinicaltrials.gov/ct2/show/NCT04468529
62. Lonsdale, J. et al. The genotype-tissue expression (GTEx) project. *Nat. Genet.* **45**, 580–585 (2013).
63. Ge, T., Chen, C.-Y., Ni, Y., Feng, Y.-C. A. & Smoller, J. W. Polygenic prediction via Bayesian regression and continuous shrinkage priors. *Nat. Commun.* **10**, 1776 (2019).
64. Karlson, E. W., Boutin, N. T., Hoffnagle, A. G. & Allen, N. L. Building the Partners HealthCare Biobank at Partners Personalized Medicine: informed consent, return of research results, recruitment lessons and operational considerations. *J. Pers. Med.* **6**, 2 (2016).
65. Nagai, A. et al. Overview of the BioBank Japan project: study design and profile. *J Epidemiol* **27**, S2–S8 (2017).
66. Sakaue, S. et al. Dimensionality reduction reveals fine-scale structure in the Japanese population with consequences for polygenic risk prediction. *Nat. Commun.* **11**, 1569 (2020).
67. McElhinney, D. B., Geiger, E., Blinder, J., Benson, D. W. & Goldmuntz, E. *NKX2.5* mutations in patients with congenital heart disease. *J. Am. Coll. Cardiol.* **42**, 1650–1655 (2003).
68. Orr, N. et al. A mutation in the atrial-specific myosin light chain gene (*MYL4*) causes familial atrial fibrillation. *Nat. Commun.* **7**, 11303 (2016).
69. Bakker Martijn, L. et al. Transcription factor Tbx3 is required for the specification of the atrioventricular conduction system. *Circ. Res.* **102**, 1340–1349 (2008).
70. Bruneau, B. G. Signaling and transcriptional networks in heart development and regeneration. *Cold Spring Harb. Perspect. Biol.* **5**, a008292 (2013).
71. Hoogaars, W. M. H. et al. Tbx3 controls the sinoatrial node gene program and imposes pacemaker function on the atria. *Genes Dev.* **21**, 1098–1112 (2007).
72. Boogerd, C. J. & Evans, S. M. TBX5 and NuRD divide the heart. *Dev. Cell* **36**, 242–244 (2016).
73. Mori, A. D. & Bruneau, B. G. *TBX5* mutations and congenital heart disease: Holt-Oram syndrome revealed. *Curr. Opin. Cardiol.* **19**, 211–215 (2004).
74. Mesbah, K., Harrelson, Z., Théveniau-Ruissy, M., Papaioannou, V. E. & Kelly, R. G. Tbx3 is required for outflow tract development. *Circ. Res.* **103**, 743–750 (2008).
75. Xie, H. et al. Identification of *TBX2* and *TBX3* variants in patients with conotruncal heart defects by target sequencing. *Human Genomics* **12**, 44 (2018).
76. van Eif, V. W. W., Devalla, H. D., Boink, G. J. J. & Christoffels, V. M. Transcriptional regulation of the cardiac conduction system. *Nat. Rev. Cardiol.* **15**, 617–630 (2018).
77. Juillière, Y. et al. Additional predictive value of both left and right ventricular ejection fractions on long-term survival in idiopathic dilated cardiomyopathy. *Eur. Heart J.* **18**, 276–280 (1997).
78. Udler, M. S. et al. Type 2 diabetes genetic loci informed by multi-trait associations point to disease mechanisms and subtypes: a soft clustering analysis. *PLoS Med.* **15**, e1002654 (2018).

The BioBank Japan Project

Koichi Matsuda[23,24], Yuji Yamanashi[25], Yoichi Furukawa[26], Takayuki Morisaki[27], Yoshinori Murakami[28], Yoichiro Kamatani[11,12], Kaori Mutu[29], Akiko Nagai[29], Wataru Obara[30], Ken Yamaji[31], Kazuhisa Takahashi[32], Satoshi Asai[33,34], Yasuo Takahashi[34], Takao Suzuki[35], Nobuaki Sinozaki[35], Hiroki Yamaguchi[36], Shiro Minami[37], Shigeo Murayama[38], Kozo Yoshimori[39,40], Satoshi Nagayama[41], Daisuke Obata[42], Masahiko Higashiyama[43], Akihide Masumoto[44] and Yukihiro Koretsune[45]

[23]Laboratory of Genome Technology, Human Genome Center, Institute of Medical Science, The University of Tokyo, Tokyo, Japan. [24]Laboratory of Clinical Genome Sequencing, Graduate School of Frontier Sciences, The University of Tokyo, Tokyo, Japan. [25]Division of Genetics, The Institute of Medical Science, The University of Tokyo, Tokyo, Japan. [26]Division of Clinical Genome Research, Institute of Medical Science, The University of Tokyo, Tokyo, Japan. [27]Division of Molecular Pathology IMSUT Hospital, Department of Internal Medicine Project Division of Genomic Medicine and Disease Prevention The Institute of Medical Science, The University of Tokyo, Tokyo, Japan. [28]Division of Molecular Pathology, Institute of Medical Science, The University of Tokyo, Tokyo, Japan. [29]Department of Public Policy, Institute of Medical Science, The University of Tokyo, Tokyo, Japan. [30]Department of Urology, Iwate Medical University, Iwate, Japan. [31]Department of Internal Medicine and Rheumatology, Juntendo University Graduate School of Medicine, Tokyo, Japan. [32]Department of Respiratory Medicine, Juntendo University Graduate School of Medicine, Tokyo, Japan. [33]Division of Pharmacology, Department of Biomedical Science, Nihon University School of Medicine, Tokyo, Japan. [34]Division of Genomic Epidemiology and Clinical Trials, Clinical Trials Research Center, Nihon University School of Medicine, Tokyo, Japan. [35]Tokushukai Group, Tokyo, Japan. [36]Department of Hematology, Nippon Medical School, Tokyo, Japan. [37]Department of Bioregulation, Nippon Medical School, Kawasaki, Japan. [38]Tokyo Metropolitan Geriatric Hospital and Institute of Gerontology, Tokyo, Japan. [39]Fukujuji Hospital, Tokyo, Japan. [40]Japan Anti-Tuberculosis Association, Tokyo, Japan. [41]The Cancer Institute Hospital of the Japanese Foundation for Cancer Research, Tokyo, Japan. [42]Center for Clinical Research and Advanced Medicine, Shiga University of Medical Science, Shiga, Japan. [43]Department of General Thoracic Surgery, Osaka International Cancer Institute, Osaka, Japan. [44]Aso Iizuka Hospital, Fukuoka, Japan. [45]National Hospital Organization Osaka National Hospital, Osaka, Japan.

Methods

Study design. Except where otherwise stated, all analyses were conducted in the UK Biobank, which is a richly phenotyped, prospective, population-based cohort that recruited 500,000 individuals aged 40–69 years in the UK via mailer from 2006 to 2010 (ref. [25]). We analyzed 487,283 participants with genetic data and who had not withdrawn consent as of February 2020. Informed consent was obtained from all participants. Access to UK Biobank was provided under application no. 7089 and approved by the MGB institutional review board (IRB; protocol 2019P003144). MGB Biobank analyses were also approved by the MGB IRB. FHS participants were ascertained and enrolled with written informed consent as described previously and approved by the IRBs of Boston University Medical Center and Massachusetts General Hospital[79]. BBJ analyses were approved by the Institute of Medical Science, the University of Tokyo, as well as the cooperating hospitals[65]. Here, we provide an overview of the methods used in this manuscript, as explained in more detail below.

We manually annotated pixels from magnetic resonance images from the UK Biobank: the pulmonary artery and the left and right ventricles were annotated in the short axis view, and the RA and RV were annotated in the four-chamber long axis view. We then trained two deep learning models (one for each of the views) with our manual annotations, and applied this model to the remaining images in the UK Biobank. For the RV, we integrated the data from the four-chamber view and the short axis view to generate a surface mesh and derived the ventricular volumes from this mesh. We analyzed the relationships between each of these derived quantitative measurements of the right heart. We also analyzed their relationships with diseases and other phenotypes in the UK Biobank.

Then, we excluded people with prevalent heart failure, pulmonary hypertension, atrial fibrillation or coronary artery disease at time of enrollment and conducted GWAS of the right heart phenotypes. We performed transcriptome-wide association studies (TWAS) that incorporated publicly available gene expression data with our GWAS results to prioritize genes at most genomic loci. We analyzed the GWAS results in light of the four-chamber single nucleus sequencing data that is publicly available. We also performed a rare variant association test in UK Biobank participants with both imaging and exome sequencing data. Polygenic scores produced from SNPs associated with right heart phenotypes in the UK Biobank GWAS were used to predict incident atrial fibrillation or flutter, dilated cardiomyopathy and pulmonary hypertension in the UK Biobank participants whose data did not contribute to the GWAS. Replication of the polygenic analysis was pursued in external biobanks.

Statistical analyses were conducted with R v.3.6 (R Foundation for Statistical Computing).

Semantic segmentation and deep learning model training. Semantic segmentation is the process of assigning labels to pixels of an image. Here, we labeled pixels within specific anatomical structures (the right atrial blood pool, the right ventricular blood pool and the PA blood pool), using a process similar to that described in our previous work evaluating the thoracic aorta[33]. Segmentation of cardiovascular structures was annotated manually in four-chamber and short axis images from the UK Biobank by a cardiologist (J.P.P.). To produce the model used in this manuscript, 714 short axis images were chosen, segmented manually, and used to train a deep learning model with PyTorch v.1.6 and fastai v.1.0.61 (refs. [26,27]). The same was done separately with 445 four-chamber images.

An earlier developmental model was produced from 250 training samples for the short axis images, and the errors produced by that model informed the structures that we segmented in the 714 short axis training examples; see Supplementary Note for additional detail. For both the short axis and the four-chamber long axis views, the models were based on the U-Net-derived architecture from fastai v.1.0.61 constructed with a ResNet34 encoder, which was pretrained on ImageNet[28–30,80]. The U-Net design incorporates skip connections between downsampling and upsampling layers, allowing more precise pixel labeling. During training, random perturbations of the input images, known as augmentations, were applied; these included affine rotation, zooming and modification of the brightness and contrast. The Adam optimizer was used[81]. The models were trained with a cyclic learning rate training policy[82]. We used 80% of the samples to train the model, and 20% for validation.

For the short axis images, all images were resized initially to 104×104 pixels during the first half of training, and then to 224×224 pixels during the second half of training. The model was trained with a mini-batch size of 16 (with small images) or 8 (with large images). Maximum weight decay was 1×10^{-3}. The maximum learning rate was 1×10^{-3}, chosen based on the learning rate finder[26,83]. Because the RV and PA blood pools occupied very little of the overall short axis image area, a focal loss function was used (with alpha 0.7 and gamma 0.7), which can improve performance in the case of imbalanced labels[84]. When training with small images, 60% of iterations were permitted to have an increasing learning rate during each epoch, and training was performed over 30 epochs while keeping the weights for all but the final layer frozen. Then, all layers were unfrozen, the learning rate was decreased to 1×10^{-7}, and the model was trained for an additional ten epochs. When training with large images, 30% of iterations were permitted to have an increasing learning rate, and training was done for 30 epochs while keeping all but the final layer frozen. Finally, all layers were unfrozen, the learning rate was decreased to 1×10^{-7}, and the model was trained for an additional ten epochs.

For the four-chamber long axis images, all images were resized initially to 76×104 pixels during the first half of training, and then to 150×208 pixels during the second half of training. The model was trained with a mini-batch size of four (with small images) or two (with large images). Maximum weight decay was 1×10^{-2}. Cross entropy loss was used[85]. We permitted 30% of iterations to have an increasing learning rate during each epoch. When training with small images, the maximum learning rate was initially 1×10^{-3}, and training was performed over 50 epochs while keeping all weights frozen except for the final layer. Then, all layers were unfrozen, the learning rate was decreased to 3×10^{-5}, and the model was trained for an additional 15 epochs. When training with large images, the maximum learning rate was set to 3×10^{-4}, and the model was trained for 50 epochs while keeping all but the final layer frozen. Finally, all layers were unfrozen, the learning rate was decreased to 1×10^{-7}, and the model was retrained for an additional 15 epochs.

Held-out test sets that were not used for training or validation were used to assess the final quality of both models (as detailed in the Supplementary Note). The final short axis and four-chamber long axis models were then applied, respectively, to all available short axis images and four-chamber long axis images available in the UK Biobank as of November 2020. The techniques used to postprocess the deep learning output to measure right atrial area and PA diameter, and to perform Poisson surface reconstruction to compute right ventricular volume, are detailed in the Supplementary Note.

Genotyping, imputation and genetic quality control. UK Biobank samples were genotyped on either the UK BiLEVE or UK Biobank Axiom arrays and imputed into the Haplotype Reference Consortium panel and the UK10K+ 1000 Genomes panel[86]. Variant positions were keyed to the GRCh37 human genome reference. Genotyped variants with genotyping call rate <0.95 and imputed variants with INFO score <0.3 or minor allele frequency ≤0.005 in the analyzed samples were excluded. After variant-level quality control, 11,631,796 imputed variants remained for analysis.

Participants without imputed genetic data, or with a genotyping call rate <0.98, mismatch between self-reported sex and sex chromosome count, sex chromosome aneuploidy, excessive third-degree relatives or outliers for heterozygosity were excluded from genetic analysis[86]. Participants were also excluded from genetic analysis if they had a history of pulmonary hypertension, atrial fibrillation, heart failure or coronary artery disease documented by ICD code or procedural code from the inpatient setting before the time they underwent cardiovascular MRI at a UK Biobank assessment center. Our definitions of these diseases in the UK Biobank are provided in Supplementary Table 4.

Heritability and GWAS. For the RA, we assessed maximum area, minimum area and fractional area change. For the RV, we assessed end diastolic volume, end systolic volume, stroke volume, and ejection fraction. For the pulmonary system, we assessed the diameter of the proximal PA diameter in systole and in diastole, strain, and the pulmonary root diameter. In addition, we analyzed body surface area-indexed values for all areas and volumes (that is, excluding strain, RA FAC and RVEF, which are dimensionless). Where paired left heart phenotypes were available, we also analyzed those left heart phenotypes alone, as well as the ratio of the right heart phenotype to its corresponding left heart phenotype. The ascending aortic diameter was paired with the PA diameter; the left ventricular end diastolic volume, end systolic volume, stroke volume and ejection fraction were paired with their corresponding right ventricular counterparts.

BOLT-REML v.2.3.4 was used to assess the SNP-heritability of the phenotypes, as well as their genetic correlation with one another using the directly genotyped variants in the UK Biobank[36].

Before conducting GWAS, a rank-based inverse normal transformation was applied to the quantitative right heart traits[87]. Therefore, effect estimates are reported in dimensionless units that represent approximately 1 s.d. of the underlying trait. All traits were adjusted for age at enrollment, age and age squared at the time of MRI the first ten principal components of ancestry, sex, the genotyping array and the MRI scanner's unique identifier.

GWAS for each phenotype were conducted using BOLT-LMM v.2.3.4 to account for cryptic population structure and sample relatedness[36,37]. We used the full autosomal panel of 714,558 directly genotyped SNPs that passed quality control to construct the genetic relationship matrix (GRM), with covariate adjustment as noted above. Associations on the X chromosome were also analyzed, using all autosomal SNPs and X chromosomal SNPs to construct the GRM ($n=732{,}193$ SNPs), with the same covariate adjustments and significance threshold as in the autosomal analysis. In this analysis mode, BOLT treats individuals with one X chromosome as having an allelic dosage of 0/2 and those with two X chromosomes as having an allelic dosage of 0/1/2. Variants with association $P<5\times10^{-8}$—a commonly used threshold—were considered to be genome-wide significant.

We used the following procedure to identify distinct GWAS loci and lead SNPs for each trait. We performed LD clumping with PLINK-1.9 (ref. [88]) using the same participants used for the GWAS, rather than a generic reference panel. We outlined a 5-Mb window (–clump-kb 5000) and used a stringent LD threshold (–r2 0.001) to account for long LD blocks such as those near the Williams–Beuren locus on chromosome 7 and the Noonan syndrome locus on chromosome 12

(refs. [89–91]). With the independently significant clumped SNPs, distinct genomic loci were then defined by starting with the SNP with the strongest *P* value, excluding other SNPs within 500 kb, and iterating until no SNPs remained. The independently significant SNP with the strongest association *P* value at each genomic locus are termed lead SNPs.

Lead SNPs were tested for deviation from Hardy-Weinberg equilibrium (HWE) at a threshold of $P < 1 \times 10^{-6}$ using the exact test[88,92]. To assess whether the HWE violations affected the association signals, SNPs with HWE $P < 1 \times 10^{-6}$ were reanalyzed with *glm* in R after excluding samples that were not within the UK Biobank's centrally adjudicated subset of individuals who self-reported British ancestry and were found to be genetic inliers for the European ancestry cluster, using the same covariates as used in the BOLT-LMM model.

We performed LD score regression analysis using *ldsc* v.1.0.0 (ref. [93]). With *ldsc*, the genomic control factor (lambda GC) was partitioned into components reflecting polygenicity and inflation, using the software's defaults.

Locus plots were produced with LocusZoom[94].

Gene set enrichment analysis. Gene set enrichment analysis (GSEA) was conducted with the online GSEA platform[39] including all nine main Molecular Signatures Database (MSigDB) collections[38]. The nearest gene to each locus from Supplementary Table 8 was input into the online platform at https://www.gsea-msigdb.org/gsea/msigdb/annotate.jsp and the top 100 results were returned. The same procedure was repeated for the nearest genes from Supplementary Table 9.

Stratified LD score regression. To identify putative cell types most relevant for each GWAS trait, we performed stratified LD score regression analysis using single nucleus RNA sequencing data from Tucker et al.[93,95,96]. Cell-type-specific markers within the RA and RV were calculated separately for the nine main cell types using a *limma-voom* differential expression model on aggregated counts per individual[97]. Only individuals with greater than 25 nuclei of a given cell type were considered. Genes were sorted by *t* statistic per cell type and the top 90% of genes were used to generate LD score regression annotations[95]. SNPs within 100 kb of any gene from a specific cell type were annotated for the respective cell type using 1000 Genomes European individuals[98]. We then performed stratified LD score regression with these annotations in combination with the baseline model described in Finucane et al.[99], only including high quality HapMap3 SNPs. We used the RA cell-type-specific annotations and RV cell-type-specific annotations for the RA- and RV-specific GWAS traits, respectively.

Replication of PA diameter GWAS results in the FHS. For external replication of the UK Biobank GWAS results, we analyzed SNP associations with PA diameter in FHS, measured on computed tomography (CT) images. The genetic profiles of FHS participants were measured by the Affymetrix GeneChip 500 K Array Set and 50K Human Gene Focused Panel, and genotyping was called using BRLMM as previously described[100,101]. Variants with call rate <0.97, HWE $P < 10^{-6}$, $n > 100$ Mendelian errors or MAF < 0.01 were excluded. The remaining variants were then imputed to the TOPMed imputation panel using Michigan Imputation Server (https://imputationserver.sph.umich.edu/index.html)[102].

A multidetector CT scanner (General Electric Lightspeed plus eight detector scanner) was used to assess the PA in FHS participants[79,103]. The PA measurements and genotyping data were available from dbGaP (phs000007.v32.p13 and phs000342.v20.p13, respectively). The association between each genetic variant and CT traits was tested with linear mixed effects models using the *kinship* package in R, and adjusted for sex, age, age squared, cohort (original cohort, offspring cohort or third generation cohort) and the first five principal components of ancestry.

SNPs from the UK Biobank PA diameter in systole GWAS were clumped based on insample LD within the UK Biobank using an LD r^2 cutoff of 0.001 to identify independent signals in PLINK-1.9 (ref. [88]). A lookup of SNP effect sizes in FHS was then conducted. We applied a variety of UK Biobank GWAS *P* value cutoffs (from 5×10^{-3} to 5×10^{-10}) and then used SNPs below those cutoffs in linear models, recording the correlation between the FHS and UK Biobank SNP effect sizes and plotting the results.

For the SNPs associated in UK Biobank at $P < 5 \times 10^{-8}$, a two-tailed binomial test was performed to compare the number of directionally concordant SNP effects with that expected by chance (an expectation of 0.5 probability of concordance at each SNP).

Polygenic score analysis. For RVEDV, RVESV and RVEF, we computed polygenic scores using the software program *PRScs* (v.sha1@43128be) with a UK Biobank European ancestry LD panel made publicly available by the software authors[63]. The PRScs method applies a continuous shrinkage before the SNP weights. PRScs was run in 'auto' mode on a per chromosome basis. This mode places a standard half-Cauchy prior on the global shrinkage parameter and learns the global scaling parameter from the data; as a consequence, PRScs-auto does not require a validation data set for tuning. Based on the software default settings, only the 1,117,425 SNPs found at HapMap3 sites that were also present in the UK Biobank were permitted to contribute to the score. These scores were applied to the entire UK Biobank.

The three RV scores were tested for association with dilated cardiomyopathy using Cox proportional hazards models as implemented by the R *survival* package[104]. Participants related within three degrees of kinship to those who had undergone MRI, based on the precomputed relatedness matrix from the UK Biobank, were excluded from analysis[86]. We conducted these analyses in individuals who were 'genetic inliers' for European ancestry based on the first three pairs of genetic principal components (PC1&2, PC3&4, PC5&6) by using the *aberrant* package as described previously[86,105]. We also excluded individuals with disease that was diagnosed before enrollment in the UK Biobank. We counted survival as the number of years between enrollment and disease diagnosis (for those who developed disease) or death, loss to follow-up or end of follow-up time (for those who did not develop disease). We adjusted for covariates including sex, the cubic basis spline of age at enrollment, the interaction between the cubic basis spline of age at enrollment and sex, the genotyping array, the first five principal components of ancestry and the cubic basis splines of height (cm), weight (kg), body mass index (BMI) ($kg\,m^{-2}$), diastolic blood pressure and systolic blood pressure.

The single strongest right ventricular score was also analyzed jointly in a model that additionally accounted for a polygenic score produced using the same PRScs-auto method for the left ventricular end systolic volume indexed to body surface area (LVESVi), chosen because this phenotype was the trait that produced the strongest left ventricular polygenic score for predicting dilated cardiomyopathy[106].

The same procedure, including the application of PRScs-auto, was repeated to produce polygenic scores for the PA phenotypes, which were tested for association with pulmonary hypertension. It was also repeated to produce polygenic scores for right atrial phenotypes, which were tested for association with atrial fibrillation and flutter.

Cumulative incidence curves were plotted to demonstrate the relationship between the RVEF polygenic score and dilated cardiomyopathy, using the *survminer v.3.1-8* package. The population was split into the top 5% of the score and the remaining 95%. Another plot was produced after residualizing the RVEF polygenic score for the LVESVi polygenic score and then splitting into the top 5% and the remaining 95%. To identify violations of the proportional hazards assumptions, Schoenfeld residuals were computed for both of these models.

Reporting summary. Further information on research design is available in the Nature Research Reporting Summary linked to this article.

Data availability

UK Biobank data are made available to researchers from research institutions with genuine research inquiries, following IRB and UK Biobank approval. GWAS summary statistics are available at the Broad Institute Cardiovascular Disease Knowledge Portal (http://www.broadcvdi.org). Single nucleus RNA sequencing data are publicly available at the Single Cell Portal (https://singlecell.broadinstitute.org/single_cell accession no. SCP498). The dbGAP study accession numbers used for FHS replication were phs000007.v32.p13 for PA diameter measurement and phs000342.v20.p13 for genotyping. BBJ data are available to bona fide researchers for approved research by application to the Japanese Genotype-phenotype Archive. MGB data are available to MGB investigators. All other data are contained within the article and its Supplementary information, or are available upon reasonable request to the corresponding author.

Code availability

The code used to perform Poisson surface reconstruction from segmentation output is located at https://github.com/broadinstitute/ml4h and is available under an open-source BSD license. The code used to perform permutation testing to assess enrichment of disease-related genes near GWAS loci is located at https://github.com/carbocation/genomisc and is available under an open-source BSD license. The code used to annotate magnetic resonance images is located at https://github.com/carbocation/traceoverlay and is available under an open-source BSD license.

References

79. Is, R. et al. Distribution, determinants, and normal reference values of thoracic and abdominal aortic diameters by computed tomography (from the Framingham Heart Study). *Am J Cardiol* **111**, 1510–1516 (2013).
80. He, K., Zhang, X., Ren, S. & Sun, J. Deep residual learning for image recognition. Preprint at *arXiv* https://doi.org/10.48550/arXiv.1512.03385 (2015).
81. Kingma, D. P. & Ba, J. Adam: a method for stochastic optimization. Preprint at *arXiv* https://doi.org/10.48550/arXiv.1412.6980 (2017).
82. Smith, L. N. Cyclical learning rates for training neural networks. Preprint at *arXiv* https://doi.org/10.48550/arXiv.1506.01186 (2015).
83. Smith, L. N. A disciplined approach to neural network hyper-parameters: Part 1–learning rate, batch size, momentum, and weight decay. Preprint at *arXiv* https://doi.org/10.48550/arXiv.1803.09820 (2018).
84. Lin, T.-Y., Goyal, P., Girshick, R., He, K. & Dollár, P. Focal loss for dense object detection. Preprint at *arXiv* https://doi.org/10.48550/arXiv.1708.02002 (2018).

85. Cox, D. R. The regression analysis of binary sequences. *J. R. Stat. Soc. B Methodol.* **20**, 215–232 (1958).
86. Bycroft, C. et al. The UK Biobank resource with deep phenotyping and genomic data. *Nature* **562**, 203–209 (2018).
87. Yang, J. et al. *FTO* genotype is associated with phenotypic variability of body mass index. *Nature* **490**, 267–272 (2012).
88. Chang, C. C. et al. Second-generation PLINK: rising to the challenge of larger and richer datasets. *Gigascience* **4**, 7 (2015).
89. Osborne, L. R. & Mervis, C. B. Rearrangements of the Williams–Beuren syndrome locus: molecular basis and implications for speech and language development. *Expert Rev. Mol. Med.* **9**, 1–16 (2007).
90. Pober, B. R. Williams-Beuren syndrome. *N. Engl. J. Med.* **362**, 239–252 (2010).
91. Tartaglia, M. et al. Mutations in *PTPN11*, encoding the protein tyrosine phosphatase SHP-2, cause Noonan syndrome. *Nat. Genet.* **29**, 465–468 (2001).
92. Wigginton, J. E., Cutler, D. J. & Abecasis, G. R. A note on exact tests of Hardy-Weinberg equilibrium. *Am. J. Hum. Genet.* **76**, 887–893 (2005).
93. Bulik-Sullivan, B. K. et al. LD score regression distinguishes confounding from polygenicity in genome-wide association studies. *Nat. Genet.* **47**, 291–295 (2015).
94. Boughton, A. P. et al. LocusZoom.js: interactive and embeddable visualization of genetic association study results. *Bioinformatics* **37**, 3017–3018 (2021).
95. Finucane, H. K. et al. Heritability enrichment of specifically expressed genes identifies disease-relevant tissues and cell types. *Nat. Genet.* **50**, 621–629 (2018).
96. Tucker, N. R. et al. Transcriptional and cellular diversity of the human heart. *Circulation* **142**, 466–482 (2020).
97. Law, C. W., Chen, Y., Shi, W., & Smyth. G. K. voom: precision weights unlock linear model analysis tools for RNA-seq read counts *Genome Biol.* **15** R29 (2014).
98. Auton, A. et al. A global reference for human genetic variation. *Nature* **526**, 68–74 (2015).
99. Finucane, H. K. et al. Partitioning heritability by functional annotation using genome-wide association summary statistics. *Nat. Genet.* **47**, 1228–1235 (2015).
100. Benjamin, E. J. et al. Variants in *ZFHX3* are associated with atrial fibrillation in individuals of European ancestry. *Nat. Genet.* **41**, 879–881 (2009).
101. Hong, H. et al. Assessing batch effects of genotype calling algorithm BRLMM for the Affymetrix GeneChip Human Mapping 500 K array set using 270 HapMap samples. *BMC Bioinf.* **9**, S17 (2008).
102. Das, S. et al. Next-generation genotype imputation service and methods. *Nat. Genet.* **48**, 1284–1287 (2016).
103. Qazi, S. et al. Increased aortic diameters on multidetector computed tomographic scan are independent predictors of incident adverse cardiovascular events: the Framingham Heart Study. *Circ. Cardiovasc. Imaging* **10**, e006776 (2017).
104. Therneau, T. M. & Grambsch, P. M. *Modeling Survival Data: Extending the Cox Model.* (Springer-Verlag, 2000). https://doi.org/10.1007/978-1-4757-3294-8
105. Bellenguez, C. et al. A robust clustering algorithm for identifying problematic samples in genome-wide association studies. *Bioinformatics* **28**, 134–135 (2012).
106. Pirruccello, J. P. et al. Analysis of cardiac magnetic resonance imaging in 36,000 individuals yields genetic insights into dilated cardiomyopathy. *Nat. Commun.* **11**, 2254 (2020).

Acknowledgements

We thank all participants of UK Biobank, MGB, BBJ and FHS. We acknowledge the staff of BBJ for their assistance. Cardiac magnetic resonance images in Fig. 1 are reproduced by kind permission of UK Biobank. We acknowledge Servier Medical Art (smart.servier.com) for the right heart illustration in Fig. 1, which is licensed under a Creative Commons Attribution 3.0 Unported License (CC-BY-3.0). We also acknowledge M. O'Reilly, from Pattern at the Broad Institute, for modifying the right heart illustration and for creating the remaining graphical illustrations in Fig. 1. This work was supported by grants from the National Institutes of Health K08HL159346 (J.P.P.), R01HL092577 (P.T.E.), K24HL105780 (P.T.E.), R01HL134893 (J.E.H.), R01HL140224 (J.E.H.), K24HL153669 (J.E.H.), 5T32HL007604-35 (V.N.), T32HL007208 (S. Khurshid), R01HL128914 (E.J.B.), R01HL092577 (E.J.B.), R01HL141434 (E.J.B.), U54HL120163 (E.J.B.) and R01HL139731 (S.A.L.). This work was supported by the Fondation Leducq 14CVD01 (P.T.E.). This work was supported by a John S LaDue Memorial Fellowship (J.P.P.) and the Sarnoff Cardiovascular Research Foundation Scholar Award (J.P.P.). This work was supported by the Tailor-Made Medical Treatment Program of the Ministry of Education, Culture, Sports, Science and Technology (BBJ). This work was supported by the Japan Agency for Medical Research via JP17km0305002 (BBJ), JP17km0305001 (BBJ), JP20km0405209 (BBJ, S. Koyama, K.I., I.K.) and JP20ek0109487 (BBJ, S. Koyama, K.I., I.K.). This work was supported by student scholarships from the Dutch Heart Foundation (S.J.) and the Amsterdams Universiteitsfonds (S.J.). This work was supported by grants from the NIH/NHLBI R01HL148050 (P.N.) and R01HL127564 (P.N.), NIH/NHGRI U01HG011719 (P.N.), and Massachusetts General Hospital Fireman Chair (P.N.). This work was supported by American Heart Association grants 18SFRN34110082 (E.J.B.), 18SFRN34250007 (S.A.L.) and a Strategically Focused Research Networks grant (P.T.E.). This work was supported by the Fredman Fellowship for Aortic Disease (M.E.L.) and the Toomey Fund for Aortic Dissection Research (M.E.L.). This work was funded by a collaboration between the Broad Institute and IBM Research.

Author contributions

J.P.P. and P.T.E. conceived of the study. J.P.P. and V.N. annotated images. J.P.P. trained the deep learning models. P.D.A. performed surface reconstruction. J.P.P., V.N., M.D.C., P.D.A., S.F.F., and M.D.R.K. conducted bioinformatic analyses in UK Biobank. S. Koyama, K.I., Y. Kamatani, and I.K. performed replication analyses in BBJ. L.-C.W. performed replication analyses in MGB. H.L. performed replication analyses in FHS. J.P.P., M.E.L., and P.T.E. wrote the paper. M.N., J.W.C., S. Khurshid, C.R., S.J.J., E.J.B., P.B., P.N., K.N., U.H., S.A.L., J.E.H., and A.A.P. contributed to the analysis plan or provided critical revisions.

Competing interests

J.P.P. has served as a consultant for Maze Therapeutics. P.B. is supported by grants from Bayer AG and IBM applying machine learning in cardiovascular disease. S.A.L. receives sponsored research support from Bristol Myers Squibb/Pfizer, Bayer AG, Boehringer Ingelheim and Fitbit, has consulted for Bristol Myers Squibb/Pfizer and Bayer AG and participates in a research collaboration with IBM. K.N. is employed by IBM Research. J.E.H. is supported by a grant from Bayer AG focused on machine learning and cardiovascular disease and a research grant from Gilead Sciences. J.E.H. has received research supplies from EcoNugenics. A.A.P. is employed as a Venture Partner at GV; he is also supported by a grant from Bayer AG to the Broad Institute focused on machine learning for clinical trial design. P.T.E. received sponsored research support from Bayer AG and IBM Research. P.T.E. has also served on advisory boards or consulted for Bayer AG, Quest Diagnostics, MyoKardia and Novartis. P.N. reports investigator-initated grants from Amgen, Apple, AstraZeneca, Boston Scientific, and Novartis, personal fees from Apple, AstraZeneca, Blackstone Life Sciences, Foresite Labs, Novartis, Roche / Genentech, is a co-founder of TenSixteen Bio, is a shareholder of geneXwell and TenSixteen Bio, and spousal employment at Vertex, all unrelated to the present work. The Broad Institute has filed for a patent on an invention from P.T.E., M.E.L. and J.P.P. related to a genetic risk predictor for aortic disease. All remaining authors report no competing interests.

Additional information

Supplementary information The online version contains supplementary material available at https://doi.org/10.1038/s41588-022-01090-3.

Correspondence and requests for materials should be addressed to Patrick T. Ellinor.

Peer review information *Nature Genetics* thanks Heribert Schunkert, Eric Villard and the other, anonymous, reviewer(s) for their contribution to the peer review of this work. Peer reviewer reports are available.

Reprints and permissions information is available at www.nature.com/reprints.

nature research

Corresponding author(s): Patrick Ellinor & James Pirruccello

Last updated by author(s): Jan 16, 2022

Reporting Summary

Nature Research wishes to improve the reproducibility of the work that we publish. This form provides structure for consistency and transparency in reporting. For further information on Nature Research policies, see our Editorial Policies and the Editorial Policy Checklist.

Statistics

For all statistical analyses, confirm that the following items are present in the figure legend, table legend, main text, or Methods section.

n/a	Confirmed	
☐	☒	The exact sample size (*n*) for each experimental group/condition, given as a discrete number and unit of measurement
☐	☒	A statement on whether measurements were taken from distinct samples or whether the same sample was measured repeatedly
☐	☒	The statistical test(s) used AND whether they are one- or two-sided *Only common tests should be described solely by name; describe more complex techniques in the Methods section.*
☐	☒	A description of all covariates tested
☐	☒	A description of any assumptions or corrections, such as tests of normality and adjustment for multiple comparisons
☐	☒	A full description of the statistical parameters including central tendency (e.g. means) or other basic estimates (e.g. regression coefficient) AND variation (e.g. standard deviation) or associated estimates of uncertainty (e.g. confidence intervals)
☐	☒	For null hypothesis testing, the test statistic (e.g. *F*, *t*, *r*) with confidence intervals, effect sizes, degrees of freedom and *P* value noted *Give P values as exact values whenever suitable.*
☒	☐	For Bayesian analysis, information on the choice of priors and Markov chain Monte Carlo settings
☐	☒	For hierarchical and complex designs, identification of the appropriate level for tests and full reporting of outcomes
☐	☒	Estimates of effect sizes (e.g. Cohen's *d*, Pearson's *r*), indicating how they were calculated

Our web collection on statistics for biologists contains articles on many of the points above.

Software and code

Policy information about availability of computer code

Data collection	To annotate cardiovascular magnetic resonance images, https://github.com/carbocation/traceoverlay (sha1@c1fb020) was used.
Data analysis	- fastai v1.0.61 - pytorch v1.6 - BOLT v2.3.4 - plink 1.9 - R 3.6 - ldsc 1.0.0 - GATK 3.0 - LOFTEE 1.0 - VEP 95 - FUSION-TWAS version sha1@0ab190e - PRScs (https://github.com/getian107/PRScs) version sha1@43128be

For manuscripts utilizing custom algorithms or software that are central to the research but not yet described in published literature, software must be made available to editors and reviewers. We strongly encourage code deposition in a community repository (e.g. GitHub). See the Nature Research guidelines for submitting code & software for further information.

Data

Policy information about availability of data

All manuscripts must include a data availability statement. This statement should provide the following information, where applicable:

- Accession codes, unique identifiers, or web links for publicly available datasets
- A list of figures that have associated raw data
- A description of any restrictions on data availability

- The output of this study is a set of publicly available GWAS summary statistics keyed to GRCh37 which are available for bulk download from the Broad Institute Cardiovascular Disease Knowledge Portal (http://www.broadcvdi.org). There is no specific accession code; they are listed under "Genetic Analysis of Right Heart Structure and Function in 40,000 People".
- All cardiovascular measurements that we performed in the UK Biobank will be returned to the UK Biobank within 6 months of publication for future use by approved UK Biobank researchers.
- UK Biobank data are made available to researchers from research institutions with genuine research inquiries, following UK Biobank approval by requesting access at https://bbams.ndph.ox.ac.uk/ams/signup .
- We used publicly available single nucleus RNA sequencing data that were downloaded from https://singlecell.broadinstitute.org/single_cell accession #SCP498.
- We conducted genetic replication analyses in the Framingham Heart Study, BioBank Japan, and Mass General Brigham biobanks. Data access procedures, and where relevant accession numbers, are described below:
  - We used publicly available data from the Framingham Heart Study. These data are available to approved researchers via dbGAP study accession #phs000007.v32.p13 for pulmonary artery measurements and #phs000342.v20.p13 for genotyping. Access to dbGAP may be requested via https://dbgap.ncbi.nlm.nih.gov/aa/wga.cgi?page=login which has links detailing the reason for controlled access and the application procedure.
  - We collaborated with BioBank Japan for external replication of polygenic scores. BioBank Japan states that its data are available for specific use to bona fide researchers who may request access via the Japanese Genotype-phenotype Archive (https://www.ddbj.nig.ac.jp/jga/index-e.html)
  - We used Mass General Brigham biobank data for replication of polygenic scores. The Mass General Brigham biobank states on https://biobank.massgeneralbrigham.org/for-researchers that researchers can contact biobank@partners.org to be guided through the process of collaborating with the Mass General Brigham Biobank.

All other data are contained within the article and its supplementary information. Although no summary data have been intentionally withheld, any summary-level (non-individual level) personally identifying information is available upon reasonable request to the corresponding author.

Field-specific reporting

Please select the one below that is the best fit for your research. If you are not sure, read the appropriate sections before making your selection.

☒ Life sciences ☐ Behavioural & social sciences ☐ Ecological, evolutionary & environmental sciences

For a reference copy of the document with all sections, see nature.com/documents/nr-reporting-summary-flat.pdf

Life sciences study design

All studies must disclose on these points even when the disclosure is negative.

Sample size	45,524 UK Biobank participants had cardiac MRI data available at the time of the study. This sample size was determined by using the complete amount of data made available by the UK Biobank at the time of analysis.
Data exclusions	Exclusion criteria were pre-established: we excluded participants with known diagnosis of atrial fibrillation, coronary artery disease, or heart failure; and those without imputed genetic data, or with a genotyping call rate < 0.98, mismatch between self-reported sex and sex chromosome count, sex chromosome aneuploidy, excessive third-degree relatives, or outliers for heterozygosity as defined centrally by the UK Biobank. After quality control of the images and exclusions, we conducted GWASes of right atrial traits in 37,075 participants; of right ventricular traits in 38,251 participants; of the proximal pulmonary artery diameter in 37,073 participants; and of the pulmonary root diameter in 39,766 participants.
Replication	Replication - by which we mean in the genetics community sense of external validation - was performed in external biobanks. Replication of pulmonary artery GWAS effects was performed in FHS. Replication of polygenic scores was performed in FHS, BioBank Japan, and the Mass General Brigham Biobank. External replication (i.e., validation) was successful in the sense that the scores were successfully applied in these external datasets. The degree of agreement of each study with the UK Biobank results for each phenotype is described in detail in the manuscript.
Randomization	Randomization was not applicable to this quantitative trait genome-wide association study. Randomization is not relevant because there was no treatment to randomize.
Blinding	Sample recruitment and selection were performed centrally by the UK Biobank; the current study's investigators had no role in sample selection, and we made use of all available data that was provided by the UK Biobank. The lack of blinding is not relevant, because there was no randomized group allocation to be blinded to.

Reporting for specific materials, systems and methods

We require information from authors about some types of materials, experimental systems and methods used in many studies. Here, indicate whether each material, system or method listed is relevant to your study. If you are not sure if a list item applies to your research, read the appropriate section before selecting a response.

Materials & experimental systems

n/a	Involved in the study
☒	☐ Antibodies
☒	☐ Eukaryotic cell lines
☒	☐ Palaeontology and archaeology
☒	☐ Animals and other organisms
☐	☒ Human research participants
☒	☐ Clinical data
☒	☐ Dual use research of concern

Methods

n/a	Involved in the study
☒	☐ ChIP-seq
☒	☐ Flow cytometry
☒	☐ MRI-based neuroimaging

Human research participants

Policy information about studies involving human research participants

Population characteristics	Please see Table 1 and Supplementary Figure 1 for more detail. In brief, 45,504 UK Biobank participants had at least one relevant cardiovascular measurement. 2,633 were excluded from analysis because of heart failure, pulmonary hypertension, coronary artery disease, or atrial fibrillation diagnosed prior to their UK Biobank MRI visit. Data from the remaining 41,135 individuals contributed to one or more genetic analysis. These participants were largely European in ancestry, 53% female, average age 64 years, 3% never consumed alcohol, and 62% never smoked tobacco. There were no treatment categories because this was not a clinical trial.
Recruitment	The study authors had no contact with any participant. As described by the UK Biobank investigators, individuals aged 40-69 in the UK were recruited via mailer from 2006-2010. Participants chosen to undergo magnetic resonance imaging in the UK Biobank are reported to have been chosen due to proximity to imaging centers, and otherwise at random. Several biases arise from this. The study population largely consisted of European-ancestry UK Biobank participants, limiting generalizability to other populations. In addition, volunteer-based biobanks such as the UK Biobank can differ from the general population by largely being healthier and more female (healthy volunteer bias). There is selection in terms of the requirement for survival to middle-age in order to enroll in the UK Biobank, screening out individuals with severe disease that would cause death in early life or childhood. Finally, individuals had to survive for additional time after enrollment in the UK Biobank in order to undergo MRI (i.e., MRI was not performed upon enrollment). All of these factors enrich the study population for people who are healthier than a general population.
Ethics oversight	Our analyses of UK Biobank data were approved by the Mass General Brigham Institutional Review Board.

Note that full information on the approval of the study protocol must also be provided in the manuscript.